Official journal of the JHL 2689-9620
www.light-am.com

Review Open Access

Laser-scribed graphene for sensors: preparation, modification, applications, and future prospects

Xing Liu[1,2], Fangyi Zhang[3], Qiwen Zhang[1,2], Zhengfen Wan[1,2,*] and Xi Chen[1,2,*]

Abstract

Sensors are widely used to acquire biological and environmental information for medical diagnosis, and health and environmental monitoring. Graphene is a promising new sensor material that has been widely used in sensor fabrication in recent years. Compared with many other existing graphene preparation methods, laser-scribed graphene (LSG) is simple, low-cost, environmentally friendly, and has good conductivity and high thermal stability, making it widely used in the sensor field. This paper summarizes existing LSG methods for sensor fabrication. Primary LSG preparation methods and their variants are introduced first, followed by a summary of LSG modification methods designed explicitly for sensor fabrication. Subsequently, the applications of LSG in stress, bio, gas, temperature, and humidity sensors are summarized with a particular focus on multifunctional integrated sensors. Finally, the current challenges and prospects of LSG-based sensors are discussed.

Keywords: Graphene, Graphene oxide, Laser-scribed graphene, Sensors

Introduction

With the development of the information era, sensors capable of transmitting and detecting information have become a popular means of obtaining information. Recently, graphene materials have received increasing attention for sensor applications owing to their excellent electrical conductivity and physical, optical, thermal, and structural properties[1]. These applications mainly include the detection of physical properties such as pressure[2] and mechanical strain[3], chemical substances such as glucose[4], dopamine[5], proteins[6], heavy metals[7], and organic pollutants[8], as well as the detection of gases[9], temperature[10], and humidity[11].

Graphene has been prepared using a variety of methods such as mechanical exfoliation[12], chemical vapor deposition (CVD)[13,14], epitaxial growth[15], and chemical reduction of graphene oxide[16,17]. High-quality graphene can be obtained by mechanical exfoliation, but the low efficiency of this method prevents the large-scale production of graphene[18]. CVD is considered the most promising method for preparing large-area and high-quality graphene, but the CVD method is constrained by its high energy consumption and cost[19]. Graphene films prepared using the epitaxial growth method exhibited good electrical conductivity and high optical transmittance. However, these methods require high-temperature processing, high energy consumption, and high transfer cost[20]. Chemical reduction of graphene oxide is low cost and highly efficient, but creates environmental pollution problems

Correspondence: Zhengfen Wan (zhengfen.wan@usst.edu.cn) or Xi Chen (xichen@usst.edu.cn)
[1]Institute of Photonic Chips, University of Shanghai for Science and Technology, Shanghai 200093, China
[2]Centre for Artificial-Intelligence Nanophotonics, School of Optical-Electrical and Computer Engineering, University of Shanghai for Science and Technology, Shanghai 200093, China
Full list of author information is available at the end of the article.

during the preparation process[21]. Therefore, a low-cost, high-efficiency, and pollution-free preparation method for graphene is of great interest.

The laser direct writing technique has recently attracted research attention in various fields owing to its unique advantages of selective and localized reduction, precise and fast patterning, and the absence of masks and additional chemicals[22–26]. With the laser direct writing technique, a laser is used to irradiate the carbon precursors and generate graphene by *in-situ* scribing. The entire laser scribing process takes only a few minutes, which significantly improves the efficiency of preparing graphene[27]. Because laser-scribed graphene (LSG) films have excellent surface area, thermal stability, and electrical conductivity, they have been used in a wide variety of applications[28], including photodetectors[29], sensing[30–32], energy storage[33–36], memristors[37], holography[38], antibacterial applications[39,40] and antennas[41].

This paper reviews recent advances in sensor applications based on LSG technology is shown in Fig. 1. First, we discuss the preparation and modification of the LSG. Special attention is given to the application of LSG in various sensors and strategies for fabricating sensors with high sensitivity, a wide detection range, fast response time, and good repeatability. Subsequently, we discuss the current challenges and future developments for LSG sensors.

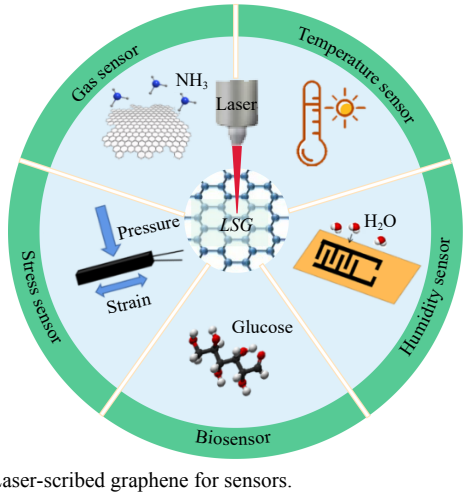

Fig. 1 Laser-scribed graphene for sensors.

Preparation and modification of laser-scribed graphene

Preparation of laser-scribed graphene

In these studies, various precursors, mainly graphene oxide (GO) and polymers, were irradiated with a laser for graphene fabrication. Different conversion processes for graphene are involved in the laser treatment. In the GO precursor, GO is converted to graphene by laser reduction, and the reduction mechanism is mainly related to the photochemical and photothermal effects of the laser; this is referred to as laser-reduced GO (LrGO)[42–45]. For polymer precursors, the direct carbonization of polymers is triggered by laser induction for graphene fabrication, referred to as laser-induced graphene (LIG)[46–49]. Graphene fabricated using these laser scribing processes has been applied to diverse graphene-based sensors. To ensure comprehensive coverage of the sensors based on both LrGO and LIG, we use the term laser-scribed graphene (LSG)[30,41,50].

Lasers for Graphene Preparation

Laser selection plays an essential role in LSG preparation. Most lasers produce photothermal effects, where GO or polymer precursors absorb and convert photon energy into thermal energy. The rapid energy deposition generates extremely high temperatures and triggers carbonization, graphitization, and exfoliation processes to form LSG[51–53]. The modification of GO or polymer precursors to graphene were reported using lasers with different wavelengths, including CO_2 infrared[54], ultraviolet (UV)[55], and visible blue-violet lasers[56]. For CO_2 infrared lasers, the infrared laser coupled to the C-C bonds in the polymer provides effective photothermal heating, and the rastering capabilities of the laser enable it to turn the LSG into any desired pattern[57]. Since the precursor has a large absorption of infrared wavelengths, the carbonization process starts as soon as the photons enter the polymer, which converts the topmost layer of the precursor into graphene[58]. Due to beam spot size and diffraction limitations, infrared lasers typically produce 60~100 μm linewidths[59]. As the wavelength decreases, the energy of the photons increases. Therefore, for UV lasers, the absorbed photon energy can directly break the chemical bonds and significantly affect the synthesis of graphene. Owing to the smaller wavelength, UV lasers can produce smaller spot sizes and have a high resolution[55]. For visible blue-violet lasers, Stanford et al. demonstrated the strong absorption of visible blue-violet photons, thus enabling visible lasers to form LSG near the surface, which results in LSG thicknesses of < 5 μm[60]. Moreover, visible lasers also take advantage of the significantly lower power, and the reduced LSG feature size extends the utility of graphene to flexible electronics and sensors.

Laser-reduced graphene oxide

GO is a precursor for LrGO, and GO films can be prepared by spin-coating, drop-casting, blade-coating, or freeze-drying on various substrates. LrGO can then be

prepared by laser reduction of the GO films[50]. Zhang et al. successfully reduced GO films by using a femtosecond laser[61]. The fabrication process of LrGO is shown in Fig. 2a. Graphene microcircuits were successfully patterned using a femtosecond laser with a computer program control system. An optical microscopy image of the graphene microcircuit is shown in Fig. 2b, c, where the reduced GO films turned black. Fig. 2d–g shows the characterization of the generated LrGO using X-ray photoelectron spectroscopy (XPS), C1s XPS spectra of GO and LrGO, X-ray diffraction (XRD), and Raman spectroscopy, respectively. As shown in Fig. 2d, e, the intensity of the O1s peak is significantly reduced after reduction compared to GO, and the decrease in C-O and increase in C-C indicate that the oxygen component was removed from the reduced GO. The C1s spectra of GO and LrGO correspond to the peaks of C-C, C-O and C=O, respectively. The content of carbon not bound to oxygen in LrGO film is much higher than that of GO. The XRD pattern of LrGO in Fig. 2f demonstrates that the diffraction peaks disappeared after the laser reduction of GO, which may be related to the removal of oxygen-containing groups from the GO film because the same results are shown in Fig. 2e. Fig. 2g presents the Raman spectra, where the I_D/I_G ratio indicates the degree of formation of the LrGO film. Compared with the GO film, the I_D/I_G of graphene oxide after laser reduction is slightly larger than that of the original GO film. The GO reduction mechanism has been reported to be closely related to the photochemical and photothermal effects of the laser[62]. There are two sub-processes in LrGO, namely the direct conversion of sp^3 carbon to sp^2 carbon and the removal of oxygen, both of which involve photochemical and photothermal effects. Importantly, these two coexisting sub-processes can be adjusted by tuning the laser power and scanning speed during the laser reduction process[63].

In addition to GO films, GO solutions[64], GO fibers[65], and GO aerogels[66] can be reduced to graphene using a laser. As shown in Fig. 2h, under pulsed laser irradiation, the GO solution containing ammonia changed rapidly from yellow to brown to black, indicating that the GO solution was effectively reduced after pulsed laser irradiation[64]. Fig. 2i shows that the GO fibers were region-specifically reduced by laser irradiation. The generated graphene fibers are lightweight and have high strength, electrical conductivity, and fiber mechanical flexibility[65]. GO aerogels were obtained by freeze-drying a specific concentration of an aqueous GO solution. As shown in Fig. 2j, the color of the

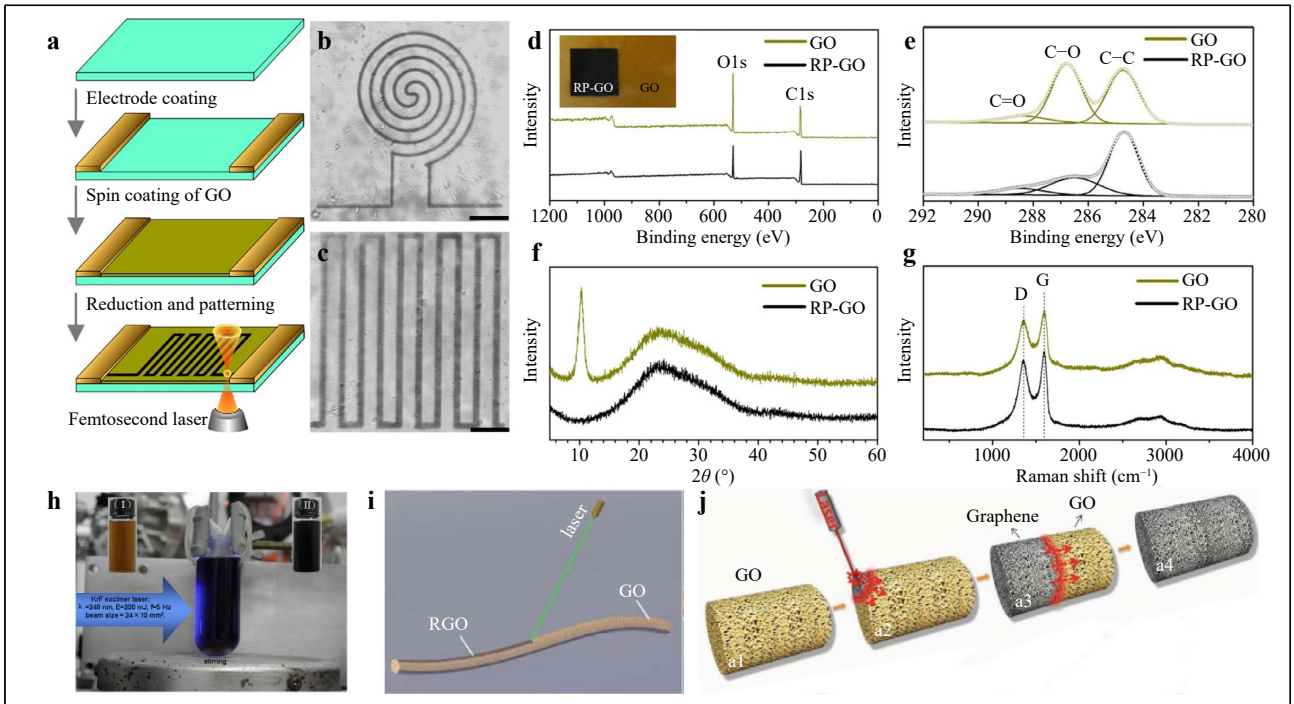

Fig. 2 a Preparation process of LrGO microcircuit on the GO film[61]. **b**, **c** Optical microscopic image of LrGO microcircuit; scale bars are 10 μm[61]. **d** Survey XPS of GO and LrGO. Inset is a photograph of an LrGO square on a GO film[61]. **e** C1s XPS spectra of GO and LrGO[61]. **f** XRD spectra of GO and LrGO[61]. **g** Raman spectra of GO and LrGO[61]. **h** Experimental device of laser-reduction system. The inset is optical images of GO solution (15 mL, 0.1 mg/mL) before (left) and after (right) pulsed-laser irradiation[64]. **i** Schematic diagram of GO fiber reduced by laser[65]. **j** Schematic diagram of graphene bulk preparation by reducing GO aerogel using laser irradiation[66].

GO aerogel quickly changed from tan to black after laser irradiation and was reduced to bulk graphene in only a few tens of milliseconds[66]. Materials prepared using LrGO have low fabrication costs and exhibit extraordinary performance in sensors, energy conversion, and storage devices.

Laser-induced graphene

Graphene can also be fabricated by laser irradiation of polymer precursors. In 2014, Lin et al. applied a CO_2 infrared laser to generate patterned porous LIG films on polyimide (PI), as shown in Fig. 3a[67]. Fig. 3b shows the scanning electron microscope (SEM) image of LIG, which can be obtained very quickly with any geometrical pattern using computer pre-programming. This method fabricated LIG in a short time using the roll-to-roll process. The magnified SEM image of LIG in Fig. 3c shows the porous foam structure of the LIG film caused by the rapid release of gas generated during laser scribing. The cross-sectional SEM image of the LIG film in Fig. 3d shows that the structure can increase the surface area of LIG and helps the electrolyte penetrate the active material. Fig. 3e shows the Raman spectra of LIG compared to the original PI demonstrating a 2D Raman band centered at 2700 cm^{-1}, a typical band found in 2D graphite, indicating a high degree of graphene formation. The XRD of LIG is Fig. 3f shows an intense peak at $2\theta = 25.9°$, indicating its high degree of graphitization. Since the energy of laser irradiation generates localized high temperatures (> 2500 ℃), it breaks the C-O, C=O, and N-C bonds, and these atoms are recombined and released as gases. The aromatic compounds are then rearranged to form a graphite structure. Therefore, LIG can be easily fabricated, has excellent commercialization potential without the need for additional chemical or high-temperature processing, and can be used for large-scale production[68].

In addition to PI precursors, LIG can also be realized using other synthetic polymers and natural materials. Diverse substrates, including leaves[51], cork[69], nail polish[70], wood[72], paper[71,73], lignin[74], coconut shells[75], phenolic resins[76], and polydimethylsiloxane (PDMS)[77], can be transformed into graphene directly by laser irradiation. Carvalho et al. developed a piezoresistive sensor for gait analysis by directly synthesizing LIG on a cork insole (Fig. 3g)[69]. Zhang et al. generated graphene with butterfly patterns on nail polish-coated Polyethylene terephthalate (PET) films via laser scribing (Fig. 3h)[70]. Kulyk et al.

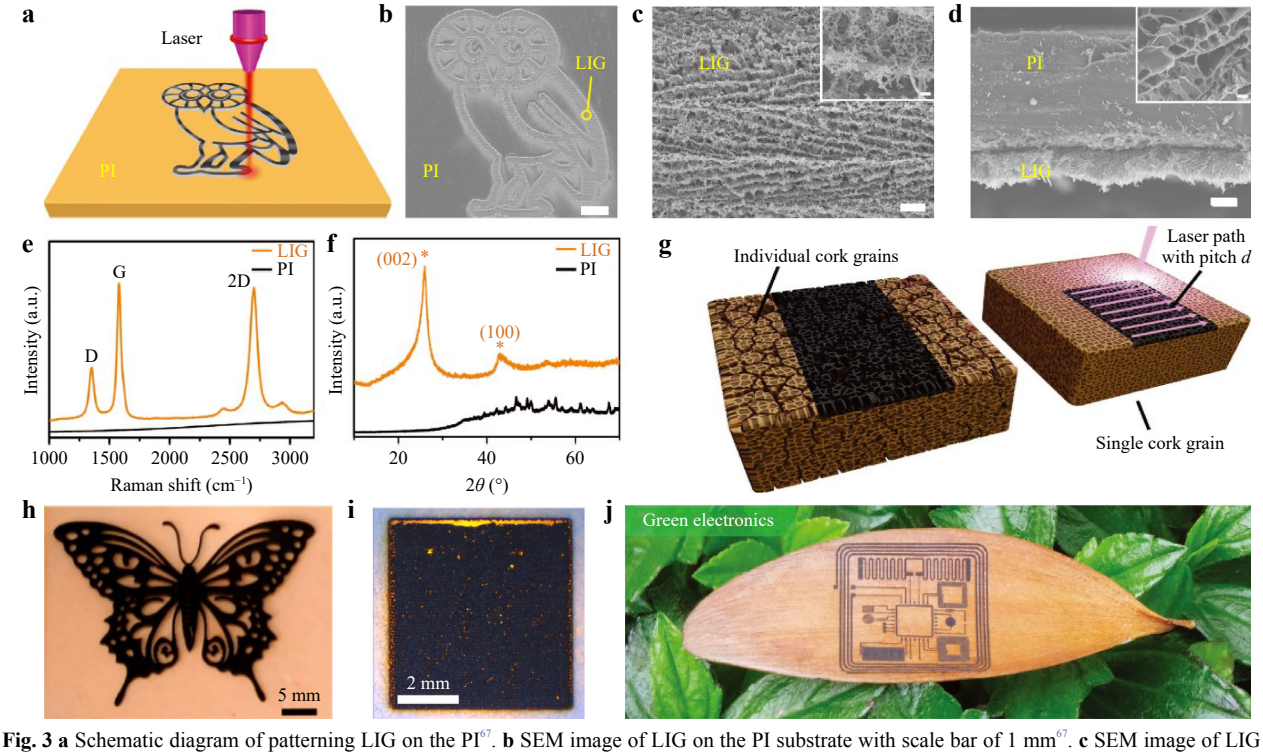

Fig. 3 **a** Schematic diagram of patterning LIG on the PI[67]. **b** SEM image of LIG on the PI substrate with scale bar of 1 mm[67]. **c** SEM image of LIG circled in **b** with higher magnification and scale bar of 1 μm[67]. **d** SEM image of the cross-section of LIG film on PI; scale bar is 20 μm. Inset shows porous morphology of LIG; scale bar is 1 μm[67]. **e** Raman spectra of LIG and original PI[67]. **f** XRD of LIG and original PI[67]. **g** Schematic diagram of LIG synthesis on a single cork[69]. **h** Schematic diagram of LIG for butterfly pattern synthesis on nail polish[70]. **i** Filter paper was irradiated by laser to synthesize LIG at laser scan line separations of 30 μm[71]. **j** Schematic diagram of LIG microcircuit synthesis on leaves[51].

reported the one-step laser-scribed synthesis of graphene on paper (Fig. 3i)[71]. By reducing the laser scan spacing, the paper damage can be reduced. Only the paper was charred on the periphery of the laser scan line, and the charred area was more resistant to laser damage. Therefore, reducing the laser scan spacing allows the next scan line to scan the charred area, forming graphene without ablation. As shown in Fig. 3j, Kim et al. synthesized a graphene microcircuit on a leaf using a high-repetition-rate UV femtosecond laser in an oxygen-free environment, and the leaf remained flexible[51]. The obtained LIG exhibited good conductivity (sheet resistance of 10 ω sq^{-1}) and high graphical resolution (line width of 40 μm).

Modification of laser-scribed graphene

The surface morphologies and properties of LSG can be tuned by adjusting the laser parameters, controlling the reduction atmosphere, and doping, which has been reported as follows.

Laser parameter adjustment and atmosphere

The surface morphology, carbonization characteristics, and wettability of LSG could be modified by varying the laser power, scanning speed, and pulse repetition frequency. Different combinations of laser parameters, such as needle, sheet, and porous, can be applied to produce different surface morphologies[78]. A high scanning speed and pulse repetition frequency help improve surface hydrophilicity[79]. Moreover, the two sub-processes of the direct conversion of sp^3 carbon to sp^2 carbon and removal of oxygen in LSG formation can be tuned by adjusting the power and scanning speed of the laser[63]. Furthermore, the number of oxygen-containing groups can be controlled by the laser power, which contributes to the performance improvement of LSG-based sensors. Importantly, highly crystalline graphitic carbon structures were successfully prepared using defocused femtosecond laser pulses, rather than focused scribing PDMS, and its conductivity was significantly improved (51.6 S m^{-1}) compared to that of a previous method without scatter-focusing (18.9 S m^{-1})[80].

Both hydrophobicity and hydrophilicity of LSG can be achieved by preparing LSG under different atmospheres. Li et al. found that LSG synthesized in O_2 or air had a water contact angle of 0°, indicating a superhydrophilic surface. When the preparation process was performed in Ar or H_2, the water contact angle of LSG was more than 150°, and the surface of LSG became superhydrophobic[81]. The LSG samples prepared in the O_2 chambers had relatively high O and C-O contents. A higher O content indicated that the LSG samples favor interaction with water, and thus became more hydrophilic. Interestingly, superhydrophilicity was maintained after one year. In contrast, Choudhury et al. first prepared LSG and then ozonated it with a UV-ozone cleaner[82]. When LSG was exposed to an O_3 atmosphere, O_3 diffused favorably into the interior of the material owing to the high specific surface area and large porosity of LSG and then further reacted with carbon atoms to produce a higher content of oxygen-containing groups such as ketone groups, hydroxyl groups, and esters at the base and edges of the material[83]. This method increased the electrochemically active surface area and porosity, thus improving ion-sensing performance.

Both methods are attributed to modifications in the surface chemistry. Once the LSG material comes into contact with water molecules, the abundant oxygen-containing groups of this material rapidly form a large number of hydrogen bonds with the water molecules, which increases its hydrophilicity to some extent.

Doping

Doping is considered to be an effective method for improving the range and sensitivity of LSG-based sensors. The main doping methods for LSG can be divided into *in situ* and postprocessing doping[84].

In situ doping involves adding the desired dopant to the precursor material and irradiating it with a laser while synthesizing the doped LSG. Wan et al. prepared LSG strain sensors with gold nanoparticles (Au NPs) doping by mixing a GO solution with $HAuCl_4$ or silver (Ag) NPs using laser irradiation, as shown in Fig. 4a–d[85]. Fig. 4e–h shows the transmission electron microscopy (TEM), SEM, and XPS results for LSG. NPs were observed on LSG, demonstrating the successful doping of Au NPs. The reduction of GO was enhanced by the local surface plasmon resonance of the Au NPs under irradiation with a 780 nm femtosecond laser. The carrier mobility (946 cm^2 V^{-1} s^{-1}) was significantly increased compared to the undoped LSG (94 cm^2 V^{-1} s^{-1}). Moreover, the doping increased the generation and extension of microcracks in the films. Ultimately, the gauge factor (GF) of the prepared LSG/Au strain sensor in the strain range of 0–25.4% was as high as 52.5.

In the same principle, as shown in Fig. 4i, Liu et al. prepared strain sensors of Platinum (Pt) NP-doped LSG simultaneously by the UV picosecond laser irradiation of thin films formed from a mixture of polybenzimidazole (PBI) and $Pt(acac)_2$ solutions[86]. Fig. 4j shows the porous network morphology of LSG and the surface with Pt NPs. The contact between the Pt NPs and graphene formed numerous conducting channels and increased the number of microcracks, thereby significantly improving the performance of the stress sensor. In addition to metal NP doping, Gong et al. used polystyrene (PS) NP-doped LSG to separate stacked graphene fragments and create

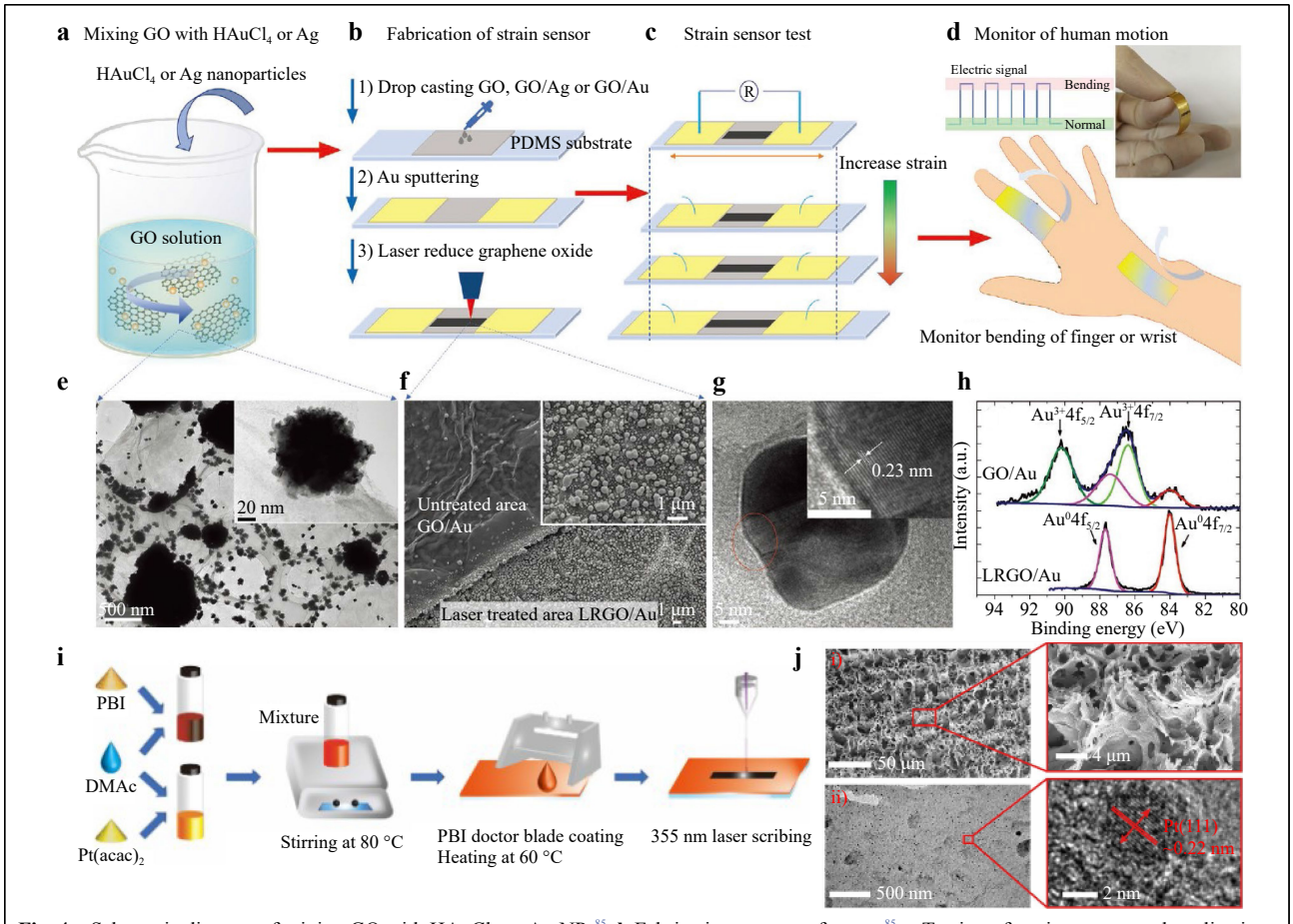

Fig. 4 a Schematic diagram of mixing GO with $HAuCl_4$ or Ag NPs[85]. **b** Fabrication process of sensor[85]. **c** Testing of strain sensors and applications in human motion monitoring[85]. **d** Inset of image shows a photograph of strain sensor[85]. **e** TEM image of LSG/Au; scale bar is 500 nm. Inset is an enlarged image; scale bar is 20 nm[85]. **f** SEM aerial view of partially laser-treated GO/Au; scale bar is 1 μm. Inset is an overall SEM image of laser-treated area; scale bar is 1 μm[85]. **g** TEM image of LSG/Au and its magnification; scale bar is 5 nm[85]. **h** Comparison of Au4f XPS spectra of GO/Au and LSG/Au (power: 5 mW, scan speed: 5 μm s^{-1})[85]. **i** Schematic diagram of Pt/LSG fabrication[86]. **j** Morphological graphs: i) field-emission gun scanning electron microscope (FEG-SEM) images of LSG tracks at a laser fluence of 25.2 mJ/cm^2. ii) TEM image of Pt supported on LSG flakes[86].

conductive channels, which significantly increased the resistance change under strain[87]. Through optimization, the GF of the doped LSG was found to be as high as 250, which is much higher than that of undoped LSG.

Post-processing doping refers to the synthesis of LSG followed by the modification of LSG with doping materials. Tehran et al. first used the electrochemical deposition technique to electrochemically deposit nanocubic-structured copper (CuNCs) on LSG, which increased the electrode surface area and improved the charge transfer rate, thus improving the electrochemical performance of the LSG glucose sensor[88]. Furthermore, as shown in Fig. 5a, Meng et al. deposited a conductive polymer poly (3, 4-ethylene dioxythiophene) (PEDOT), on LSG[89]. Fig. 5b shows the successful deposition of PEDOT onto the porous structure of the LSG. As a conductive polymer binder, PEDOT can improve the stability of the structure by enhancing the porosity of the LSG material, and its inherent electronic/ionic conductivity can improve the electrochemical performance of LSG sensors. However, with this method, the doping materials are mainly concentrated on the LSG surface, and only a small amount of dopant penetrates the LSG, resulting in a nonuniform and insufficient dopant concentration distribution[84].

Interestingly, doping can also be performed using sunlight, as shown in Fig. 5c. Prabhakaran et al. drop-casted $Cu(OAc)_2$ onto the electrode of LSG and then irradiated it with focused sunlight, which caused the rapid decomposition and oxidation of $Cu(OAc)_2$ into copper oxide nanoparticles (CuO NPs) that were anchored on the surface of the LSG electrode[90]. CuO NPs can accelerate the

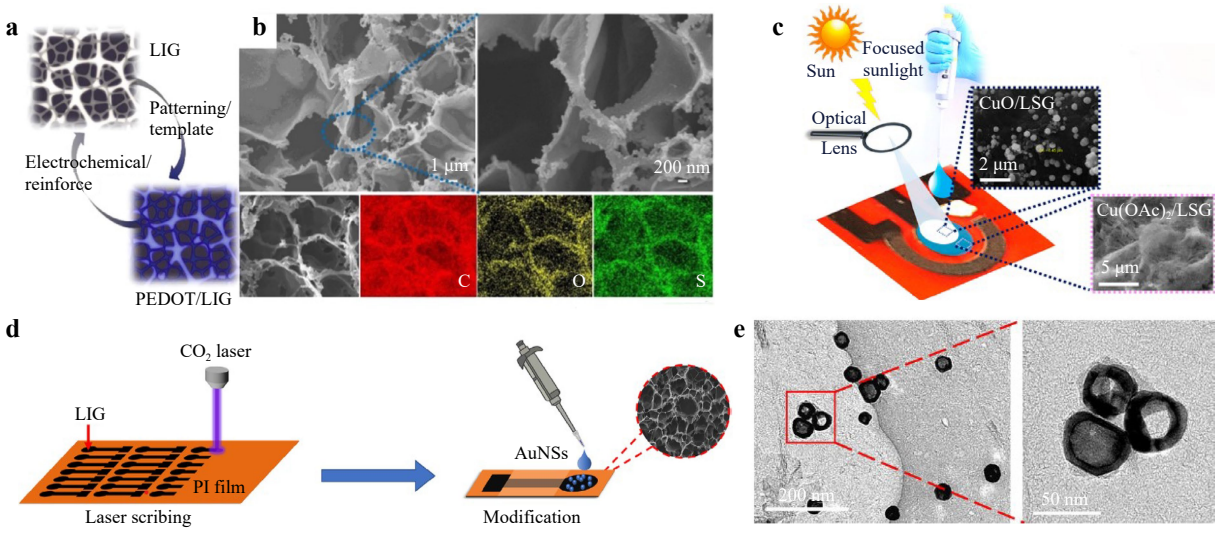

Fig. 5 a Schematic diagram of PEDOT deposition on LSG[89]. **b** SEM image and energy-dispersive X-ray spectroscopy (EDS) image after PEDOT deposition[89]. **c** Schematic diagram of CuO NPs deposited on LSG working electrode by focused sunlight; inset is a field emission scanning electron microscope of CuO deposited on LSG[90]. **d** Fabrication of AuNSs/LSG electrodes[91]. **e** TEM of AuNSs deposited on LSG[91].

transfer of electrons, thus improving the sensing performance. The drop-casting method has also been used for postprocessing doping. As shown in Fig. 5d, Qiu et al. drop-casted gold nanoshells (AuNSs) directly onto the surface of LSG for simple and rapid electrochemical detection of sulfonamides (SAs)[91]. Fig. 5e shows a TEM image of AuNSs successfully deposited on LSG. The AuNS-modified LSG electrode had a smaller semicircle and larger effective surface area than the unmodified LSG electrode, and the electrocatalytic activity of AuNSs improved the LSG sensitivity to the detector.

Applications

Stress sensors

Stress sensors detect force signals, such as tensile force, pressure, and strain, by converting them into relevant electrical signals. In fact, owing to the outstanding conductivity, high specific surface area, and excellent mechanical properties of LSG[92], LSG can respond to various forms of externally applied stress, such as the touch of a human finger, changes in physiological motion, or vibrations of vocal cords, and convert them into electrical signals for detection, making LSG-based stress sensors suitable for tactile sensing[93], health monitoring[94,95], soft robots[96], sound sensing[97], and other related applications. In recent years, the working mechanism of LSG-based stress sensors has mainly been based on the amount of variation in capacitance or resistance and generation of friction to generate electrical signals[98–100]. In this section, LSG-based stress sensors are described in detail.

LSG sensors based on capacitance variation work as follows. When stress is applied to the LSG sensor, the sensor electrode distance varies; thus, the capacitance of the sensor changes[101]. Compared to LSG stress sensors based on resistance variations, capacitance stress sensors are unaffected by the large amount of heat generated owing to resistance variations; therefore, LSG stress sensors based on capacitance variations have good temperature stability and long service life.

In addition to the above advantages, LSG stress sensors based on capacitance variations have very little electrostatic gravitational force between the charged electrodes, and therefore require very little energy, making them particularly suitable for detecting small strain ranges. As shown in Fig. 6a–c, Han et al. reported a flexible stress sensor based on capacitance variation with an interdigitated capacitive (IDC) structure[102]. Because of the increased bending of the sensor, the gap between the interdigitated electrodes increased, which enhanced the impedance. This sensor showed good linearity over a strain range of 0–3.3%, with a GF of 0.47. However, the sensitivity of this capacitance stress sensor can be improved by introducing a dielectric layer between the graphene electrodes. As shown in Fig. 6d, Huang et al. proposed a flexible capacitance pressure sensor (FCPS) based on a plate-foam-plate integrated structure[103]. The high porosity of the PDMS foam dielectric layer enabled the sensor to deform more easily under an external pressure, leading to easier capacitance changes. The PDMS foam-based pressure

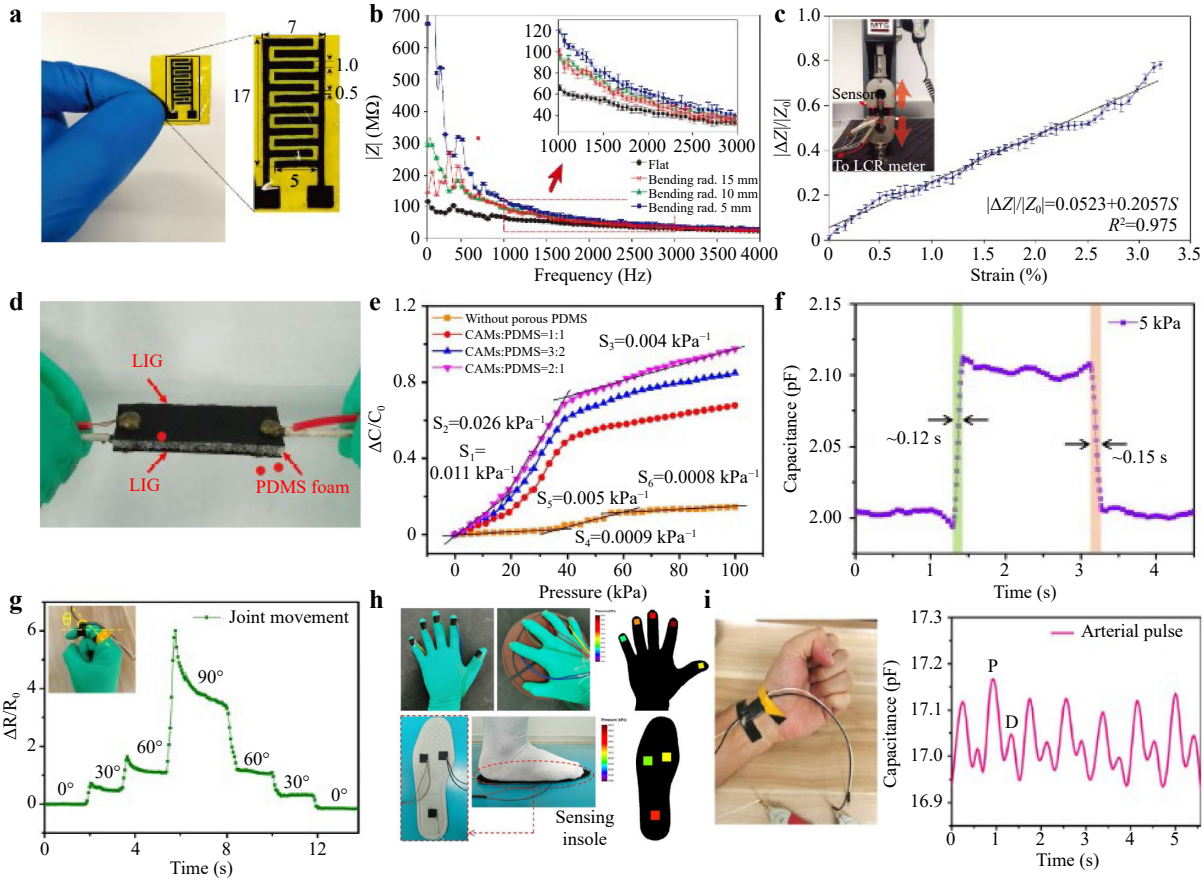

Fig. 6 **a** Schematic diagram of flexible capacitance sensor, with dimensions in millimetres[102]. **b** Response of sensor for different bending radii of curvature[102]. **c** Change in sensor impedance for different strain values applied in direction illustrated in inset[102]. **d** Schematic diagram of FCPS structure[103]. **e** Pressure response of FCPS with different ratios of citric acid monohydrate (CAMS): PDMS[103]. **f** FCPS response/relaxation time[103]. **g** The detection of joint movements[103]. **h** Pressure detection of human fingers and foot soles[103]. **i** Wrist pulse detection[103].

sensor exhibits a high sensitivity of 0.026 kPa^{-1} and a response/relaxation time of 0.12 s/0.15 s at 15–40 kPa, as shown in Fig. 6e, f. Fig. 6g–i shows that the sensor performs excellently in various applications, such as pulse monitoring, finger touch, and foot-stance analysis.

In contrast to LSG stress sensors based on capacitance variation, those based on resistance variation are widely used, because their resistance varies regularly with the applied external stress, making it easy to obtain a linear expression of the stress signal[96]. For LSG stress sensors based on resistance changes, setting the initial resistance of the sensor is crucial for determining the sensitivity of the sensor. To facilitate this, Zhu et al. proposed a stress sensor based on resistance variation with an asymmetric two-layer structure[104], as shown in Fig. 7a–c. The length, width, and spacing of the interdigital electrodes can be used to control the initial resistance. With the appropriate electrode parameters, the asymmetrically structured sensor had a sensitivity of up to 2 kPa^{-1}, a response time as short as 0.15 ms, and detected the pulse in real time. Zhao et al. also adopted a similar asymmetric structure; for the first time, LSG was scraped into powder for ink preparation, and then an asymmetric structure pressure sensor was fabricated on the substrate using screen printing technology[105]. LSG-based inks can be conveniently patterned for electrodes and are controllable. As shown in Fig. 7d, e, the prepared pressure sensor exhibited high sensitivity, fast response time/relaxation time (4 ms/5 ms), and stability after more than 1200 cycles at a pressure of 300 Pa. Owing to these excellent properties, LSG-based inks can detect fine motion in humans, recognize sound in real time, and achieve multi-touch sensing.

Zhao et al. further doped LSG based on an asymmetric structure, dispersed carbonitride (MXene) in the liquid precursor of PI, and stirred the mixture well to form uniformly dispersed doped polyimide films; doped MXene/LSG was then produced by laser irradiation[106]. Fig. 8a illustrates the preparation process of the sensor, in

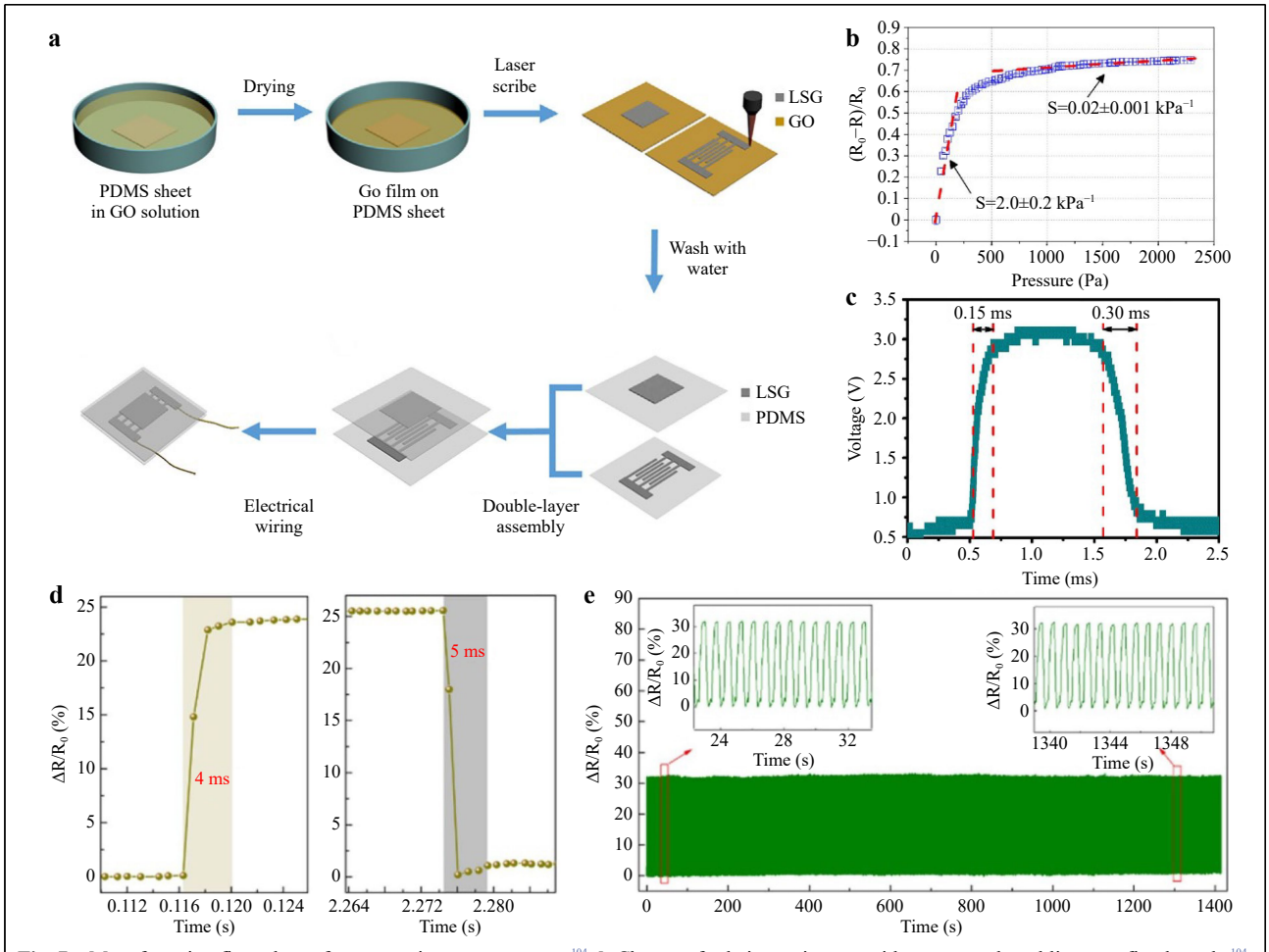

Fig. 7 a Manufacturing flow chart of asymmetric structure sensor[104]. **b** Change of relative resistance with pressure; dotted lines are fitted results[104]. **c** Response to pulse pressure[104]. **d** Response/relaxation time[105]. **e** Sensor stability and durability test; insets show two partially magnified views of cyclic curve[105].

which LSG and MXene were added, and the synergistic effect between them was beneficial for improving the sensitivity of the sensor. MXene/LSG exhibits a layer-by-layer cross-linked structure, as shown in Fig. 8b. When an external force was applied, the contact area increased, more conductive paths were created, and the resistance decreased. Simultaneously, the deformation of the internal pores caused by the MXene/LSG layer-by-layer crosslinked structure led to an increase in the contact area between the interiors. When the external force disappeared, the MXene/LSG layer-by-layer crosslinked structure returned to its original state. This MXene/LSG layer-by-layer crosslinked structure improved the sensitivity (2.25 kPa^{-1}, 0–200 Pa) of the sensor, as shown in Fig. 8c. In addition, the team uniformly dispersed multiwalled carbon nanotubes (MWCNTs) grown by one-dimensional CVD in a liquid precursor of PI and scribed the MWCNT/LSG hybrid pressure sensor with a laser[107]. As shown in Fig. 8d, MWCNT/LSG had an apparent porous structure and 3D graphene nanosheets with a collapsed and wrinkled morphology after laser scribing. The MWCNT/LSG sensitivity of the sensor was 2.41 kPa^{-1} in the pressure range of 0–200 Pa, which was better than that of bare LSG (Fig. 8e). MWCNT/LSG pressure sensors were used to detect subtle movements of the human body (vocal vibration, breathing, pulse, etc.), visible in Fig. 8f–h.

Triboelectric stress sensors generate electrical signals by changing the distance between the frictional layers after external-force stimulation, thus enabling the sensing[100]. Compared with LSG stress sensors based on capacitance or resistance changes, self-powered triboelectric LSG stress sensors can only detect dynamic and non-static stress signals. However, this sensor has a high sensitivity, fast response time, and low energy consumption. To convert wasted mechanical energy into electrical energy and reduce power consumption, triboelectric nanogenerators (TENG)

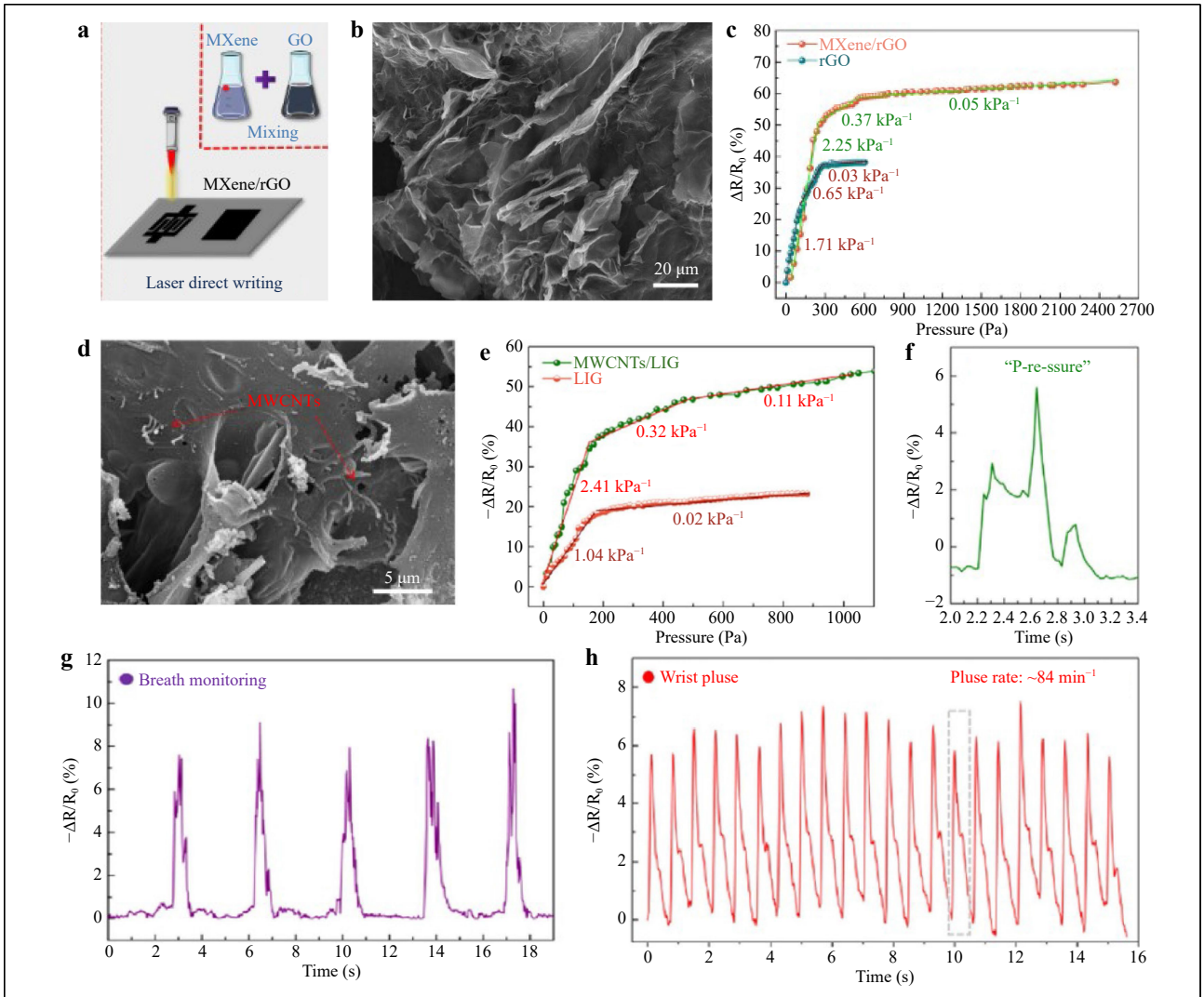

Fig. 8 a Schematic diagram of preparation process of MXene/LSG[106]. **b** SEM image of MXene/LSG[106]. **c** Sensitivity comparison of MXene/LSG and LSG asymmetric pressure sensors[106]. **d** SEM image of MWCNTs-embedded LSG[107]. **e** Sensitivity comparison of MWCNTs/LSG and LSG asymmetric pressure sensors[107]. **f** Vocal vibration[107]. **g** Breath monitoring[107]. **h** Wrist pulse monitoring[107].

have been used as triboelectric sensors[108]. Das et al. applied PDMS with a microstructure as the bottom electrode of a triboelectric sensor and attached LSG to PDMS with a polyethylene terephthalate/indium tin oxide (PET/ITO) film with triboelectric properties opposite to those of the top layer[109]. As illustrated in Fig. 9a, the PDMS contacted the PET/ITO to generate an electric charge on the surface by applying an external force. When the external force was removed, an internal electric potential was generated. Owing to the electrostatic field, the total charge was collected by the ITO and LSG, allowing the sensor to be self-powered. The resulting self-powered sensor had a response time of 9.9 ms and sensitivity of 7.69 kPa^{-1} within 0–0.5 kPa, as show in Fig. 9b, c, and was successfully applied for human posture detection. Yan et al. prepared a simple frictional tactile sensor by patterning the upper and lower LSG electrodes into a semicircle shape, and then overlapping the upper and lower layers in a complementary crossover, as shown in Fig. 9d, reducing the complexity of the sensing array and number of data channels[110]. As depicted in Fig. 9e, owing to the coupling effect of contact initiation and electrostatic induction between the top silicone rubber and LSG electrodes, an alternating current was generated when the contact-disconnection operation was repeated. Fig. 9f shows that the resistance of this self-powered tactile sensor remains essentially unchanged at different bending angles, indicating good flexibility. In addition, the sensor can maintain good performance for more than 6000 contact-separation operations under different bending angles and realize power-free tactile

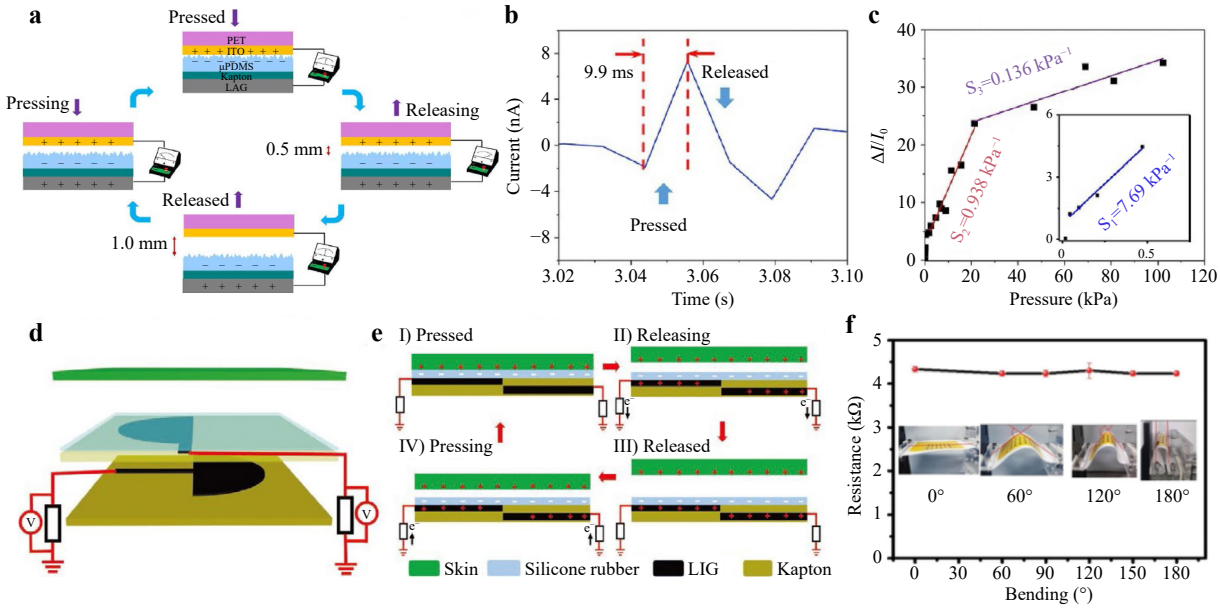

Fig. 9 a Schematic diagram of working principle of sensor[109]. **b** Response time during pressing and releasing[109]. **c** Sensitivity under different pressure conditions[109]. **d** Schematic of one sensor unit[110]. **e** Schematic diagram of working mechanism of one sensor unit[110]. **f** Resistances of patterned LSG electrode at a different bending angle[110].

sensing.

Biosensors

Biosensors are devices that convert biochemical/biological reactions into physicochemical signals for analysis, enabling quantitative assessment of analyte concentrations[68]. Biosensors can detect chemicals regarding food safety[111], environmental chemical hazards[112], and disease[113].

Detection of ions

Electroactive nanomaterials, such as carbon nanotubes (CNTs) and graphene, which have electrocatalytic activity, strong adsorption capacity, and high chemical stability during electrochemical processes, exhibit excellent performance in the detection of ions[114,115]. Nasraoui et al. reported that an electrochemical biosensor was functionalized by MWCNTs and further modified with Au NPs to detect nitrite, as shown in Fig. 10a, b[116]. To achieve a uniform and sensitive detection sensor for nitrite, MWCNTs were employed to enhance the electrical conductivity of the working electrode (WE), and Au NPs were used to improve the charge transfer resistance of the sensor to the nitrite-ionized electrolyte interface. As shown in Fig. 10c, the current increases with increasing nitrate concentration in the nitrite concentration range of 10–140 μM for electrochemical detection using square wave voltammetry (SWV). In addition, different ions could be detected by preparing LSG-based ion-selective electrodes (ISE). As shown in Fig. 10d, Kucherenko et al. scribed graphene with a CO_2 laser, passivated the middle part of the LSG to prevent the region from interfering with subsequent ion-sensing experiments, and prepared ion-selective electrodes by functionalizing LSG with ammonium ion (NH^{4+}) and potassium ion (K^+)-selective membranes to obtain NH^{4+} and K^+ sensors[117]. Fig. 10e shows the NH^{4+} detection range of 1×10^{-4}~150×10^{-3} with an average sensitivity of 51 mV^{-1} and K^+ detection range of 3×10^{-4}~150×10^{-3} with an average sensitivity of 53 mV^{-1}. Thus, the sensor can detect NH^{4+} (reference range 15–56 mmol d^{-1}) and K^+ (reference range 25–125 mmol d^{-1}) in urine and can be successfully applied to monitor hydration in patients (including elderly patients).

Detection of small biological molecules

LSG-based electrochemical biosensors can detect various small molecules, most commonly glucose[118,119], dopamine[5,32], and H_2O_2[120,121]. Settu et al. prepared a biosensor for glucose detection by immobilizing chitosan-glucose oxidase (GOx) on the surface of an LSG electrode[122]. Yoon et al. modified the LSG electrode surface using acetic acid to increase conductivity and effectively reduce sheet resistance[123]. Subsequently, Pt NPs were electrodeposited and GOx was immobilized on the surface of the LSG electrode to produce a biosensor for glucose detection. Finally, changes in the pre- and postprandial glucose levels were successfully tested using the current response of the sensor. Because enzymes tend to lose

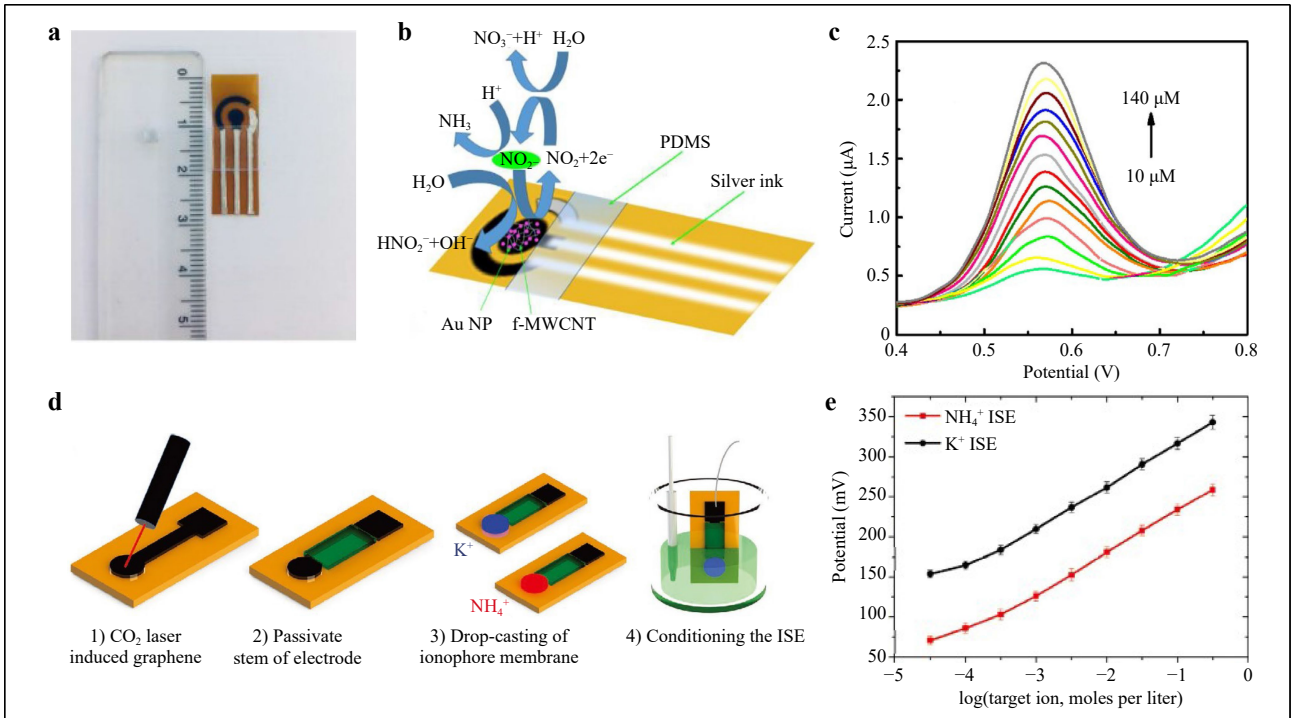

Fig. 10 a LSG/f-MWCNT-AuNPs sensors[116]. **b** Schematic representation of electro-oxidation of NO^{2-} at LSG/f-MWCNT-AuNPs[116]. **c** SWV of LSG/f-MWCNT-AuNPs electrode variation of concentration of 10–140 μM[116]. **d** Fabrication schematic of LSG ISEs[117]. **e** Calibration curves of NH^{4+} and K^+ ISEs[117].

activity or degrade, Zhu et al. reported a non-enzymatic sensor of Au/Ni/LSG WE combined with a Nafion/AgCl/Ag/LSG reference electrode (RE) and LSG counter electrode (CE) in a three-electrode configuration, as shown in Fig. 11a[124]. Fig. 11b, c shows that the encapsulation of porous Ecoflex reduces sample solution evaporation by enhancing the hydrophilicity of the porous Ecoflex and providing a weakly alkaline environment. It was also used in on-body wearable applications for glucose analysis using the sweat of healthy volunteers after meals.

Dopamine (DA) is a neurotransmitter with significant clinical diagnostic value[125]. Xu et al. reported an electrochemical sensor for detecting dopamine based on LSG modified with a PEDOT-conducting polymer, as shown in Fig. 11d[126]. DA in mixtures containing DA, ascorbic acid (AA), and uric acid (UA) was successfully detected using differential pulse voltammetry (DPV), as shown in Fig. 11e. Moreover, the linear range of DA detection was 1–150 μM, with a sensitivity of 0.220 ± 0.011 μA μM^{-1} and a detection limit of 0.33 μM.

Detecting hydrogen peroxide (H_2O_2) is useful because it is involved in diabetes, neurodegeneration, aging, and other physiological processes[127]. As shown in Fig. 11f, Aparicio-Martínez et al. developed a hydrogen peroxide sensor using Ag NPs to modify an LSG electrode[128]. For H_2O_2 detection, the sensor showed a high catalytic response to H_2O_2 reduction with a fast current response of 3 s, a wide linear range of 0.1–10 mM, and a low detection limit of 7.9 μM.

Detection of biological macromolecules

LSG-based biosensors also have great potential for detecting biological macromolecules such as nucleic acids and proteins (protein biomarkers, insulin, and proteases[129]). Detecting of nucleic acids, the essential material basis of life, is a reliable method for diagnosing infectious diseases. Wan et al. prepared a nitrogen-self-doped LSG-based biosensor by adjusting the laser power[130]. As Fig. 12a–c shows, the LSG electrode was prepared on PI using a CO_2 laser, and a specific purified microRNA (miRNA) was adsorbed directly onto the surface of the LSG electrode through miRNA extraction and magnetic separation, followed by electrochemical testing and DPV curves showed that LSG with miRNA adsorption produced a lower current than bare LSG. The sensor can detect miRNAs at concentrations as low as 10 fM. Tai et al. used Ag NP-modified LSG nanofibers. Through selective hybridization and mismatch analysis, the specific binding of the selected DNA samples captured on Ag NPs to the target DNA of Mycobacterium tuberculosis was studied to detect Mycobacterium tuberculosis[131].

Biomarkers have a wide range of applications for disease identification and diagnosis[132]. Lahcen et al. first reported the use of Au NPs and molecularly imprinted polymer

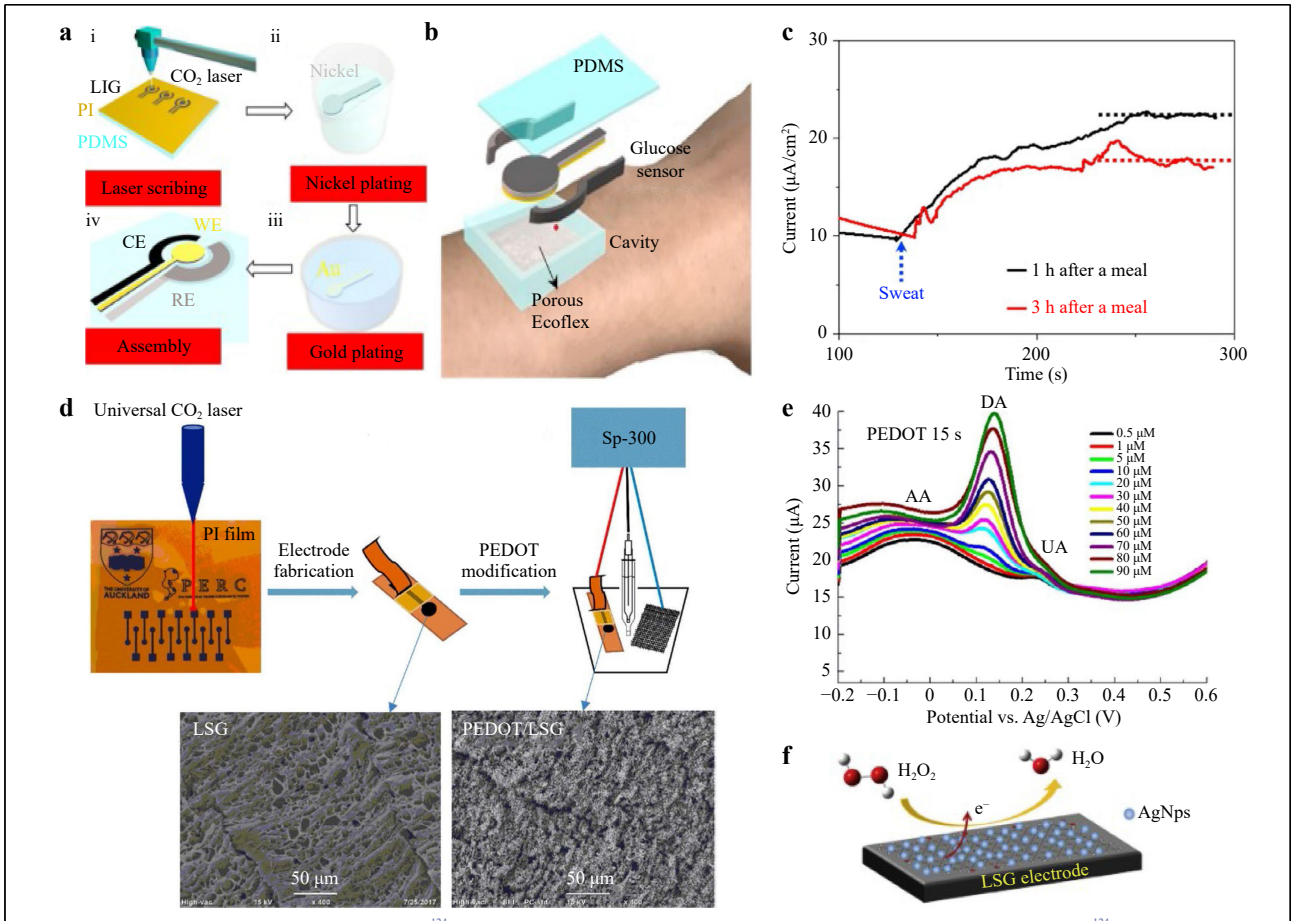

Fig. 11 **a** Preparation process of glucose sensor[124]. **b** Integration of glucose sensor and porous encapsulating reaction cavity[124]. **c** Sensor analyzes glucose in sweat of healthy volunteers 1 or 3 hours after meals[124]. **d** Preparation process of PEDOT-LSG electrode[126]. **e** DPV response of different concentrations of DA in mixture of 30×10^{-3} M AA and 4×10^{-6} M UA in PBS (pH 7.4) at 15 s PEDOT-LSG modified electrodes[126]. **f** Sensing mechanism of H_2O_2 sensor[128].

(MIP)-modified LSG electrodes for detecting the human epidermal growth factor receptor 2 (Her-2) protein, a significant breast cancer biomarker[133]. Rauf et al. prepared an aptasensor for detecting cardiac troponin-I (cTn-I) biomarkers using $ZnFe_2O_4$ NPs modified LSG[134]. Fig. 12d, e demonstrates that after cTn-I is attached, the redox reaction is hindered, and the peak current is reduced to detect cTn-I. Fig. 12f shows the SWV response. The sensor had a linear range of 0.001–200 ng/ mL with a detection limit of 0.001 ng/mL and sensitivity of 19.32 (± 0.25) μA/(ng/mL), which can be used for acute myocardial infarction screening.

Insulin is a hormone that regulates blood glucose levels; therefore, detecting the insulin concentration is essential for assessing the severity of diabetes[135]. Liu et al. were the first to report the detection of insulin using an LSG-based sensor[136]. The detection mechanism is shown in Fig. 12g–i, using a Au NP-aptamer (AuNP-Apt) and methylene blue (MB) modification to amplify the electrochemical signal of the aptamer bound to insulin, which significantly improved the sensitivity of the sensor to insulin. Finally, the insulin concentration was determined using the DPV method. This low-cost LSG electrode shows great promise for the fabrication of portable insulin sensors.

Gas, temperature, and humidity sensors

Temperature sensors

Real-time monitoring of body temperature is important for assessing the quality of various vital activities in the human body. Wearable temperature sensors with good flexibility and ductility can fit on the skin surface to ensure real-time, accurate, and comfortable body temperature monitoring, and have thus attracted wide interest[137]. Graphene has good flexibility and electrical and thermal conductivities and is widely used in wearable, flexible temperature sensors. LSG-based temperature sensors have high wearability, a fast response time, small size, etc[138]. The principle used for temperature detection is as follows.

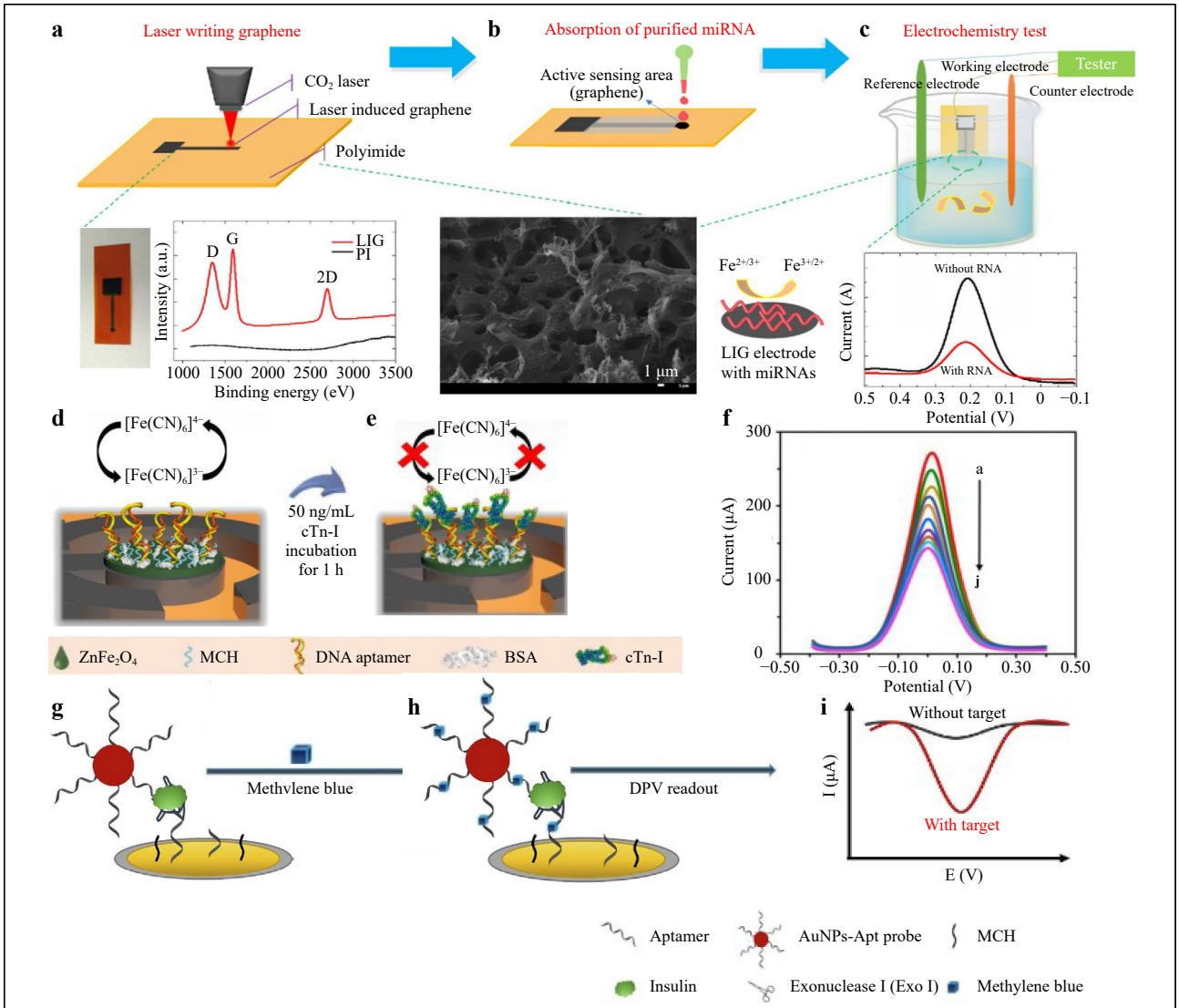

Fig. 12 a Preparation process of the LSG biosensor. Image of LSG electrode (left), Raman spectra of LSG (middle), and SEM image of LSG with scale bar of 1 mm (right)[130]. **b** Absorption process of purified target miRNA on LSG electrode surface[130]. **c** Electrochemical test of LSG electrode and DPV curve[130]. **d**, **e** Detection mechanism of cTn-I by LSG electrode[134]. **f** Use of SWV to detect cTn-I concentration, pH 7.4[134]. **g–i** Incubation with methylene blue to form MB-apt complex, and insulin measured by DPV method[136].

Graphene conducts based on two-dimensional continuous medium permeation, and the interstate mobility of carriers is proportional to temperature, making the relationship between graphene resistance and temperature a negative exponential dependence, similar to that of a negative temperature coefficient semiconductor thermistor[139]. As shown in Fig. 13a–c, Kun et al. introduced an LSG flexible temperature sensor capable of accurately measuring body temperature[140]. The temperature sensor had a linear correlation between the resistance and temperature range of the body (30–40 °C), and the resistance was stable at each temperature without fluctuations, successfully demonstrating that the LSG had an accurate and stable response to temperature. To achieve LSG with a higher sensitivity to temperature, Chen et al. systematically investigated the effect of the GO concentration and scan line spacing of the laser; the sensor structure is shown in Fig. 13d[141]. The GO concentration and scan line spacing of the laser were optimized and achieved a high sensitivity of 0.37 $℃^{-1}$ in the temperature range of 30–100 ℃. The sensor can also be used to monitor the breathing rate (Fig. 13e) and detect human blowing (Fig. 13f) and finger proximity (Fig. 13g).

To further improve the application range of LSG temperature sensors, Jung et al. prepared a temperature sensor via laser reduction and oxidation of GO on a printed

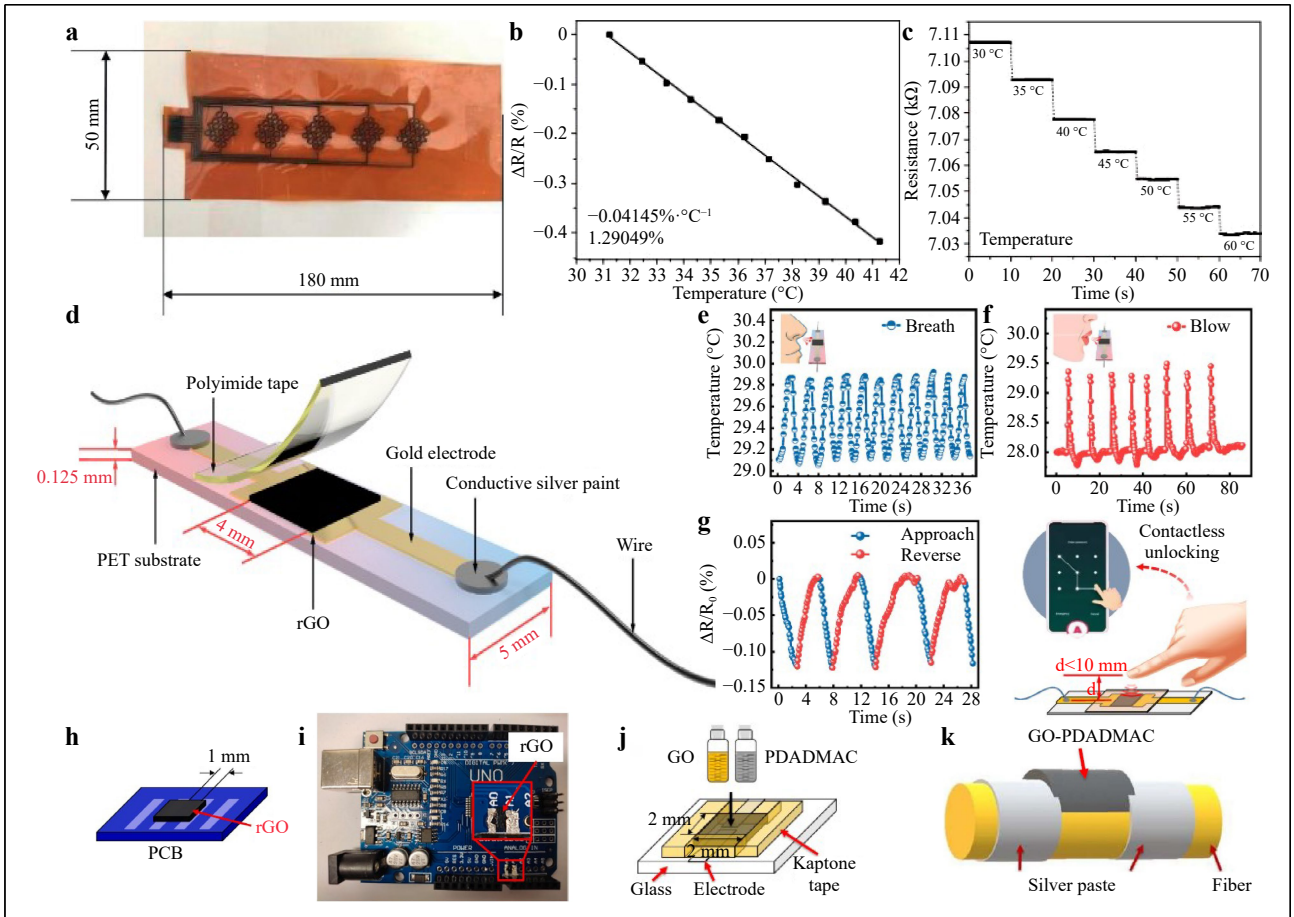

Fig. 13 **a** Schematic diagram of LSG temperature sensor[140]. **b** Linear relationship between temperature and resistance of LSG sensor for temperature range of 30–40 °C[140]. **c** Relationship between temperature and sensor resistance at different times[140]. **d** Schematic of temperature sensor[141]. **e** Breathing rate monitoring[141]. **f** Human blowing detection[141]. **g** Proximity detection experiment. Reproduced with permission[141]. **h** LSG sensor prepared on PCB with a clearance of 1 mm[142]. **i** LSG temperature sensor prepared between A_0 and A_1 pins of Arduino PCBs[142]. **j** GO-PDADMAC composites produced on glass substrate[143]. **k** Silver paste electrode between GO-PDADMAC droplets on aramid and polyester filaments[143].

circuit board (PCB), as shown in Fig. 13h, which reduced the integration complexity and improved the real-time temperature detection data[142]. Based on this process, LSG sensors were prepared on Arduino PCBs for the real-time detection of battery temperature, as shown in Fig. 13i. In addition, Jung et al. fabricated temperature sensors using LSG and poly (diallyldimethylammonium chloride) (PDADMAC) complexes that can adhere to fire suits[143]. The preparation process is shown in Fig. 13j, k, where GO and PDADMAC solutions were mixed on the glass substrate and dried; GO-PDADMAC was then placed on top of the aramid and polyester fibers, and the temperature sensor was prepared by laser reduction. Because the addition of PDADMAC can increase the hydrophobicity of the membrane and initial resistance, the temperature sensor achieved stability for one week and a sensitivity of 2.98% at room temperature.

Gas sensors

Because of the large number of 3D micro-nano porous structures of LSG, which can provide more active sites and diffusion paths for gases, thus improving the sensing performance, LSG has also been developed for gas sensors[144]. Wu et al. fabricated three parallel 3D porous graphene strips generated using laser scribing on PI to detect NH_3[145]. As shown in Fig. 14a, the middle 3D porous graphene was used as the sensing element for NH_3, and the other two were used for heating. Fig. 14b shows that the sensitivity of the sensor increases significantly as the temperature increases. However, heating the sensor to 90 ℃ and then cooling it takes a long time and affects the detection time. Therefore the sensor was heated to 70 ℃ to improve the NH_3 sensitivity of the sensor.

Stanford et al. reported an LSG gas sensor based on thermal conductivity for gas detection[146]. This sensor used

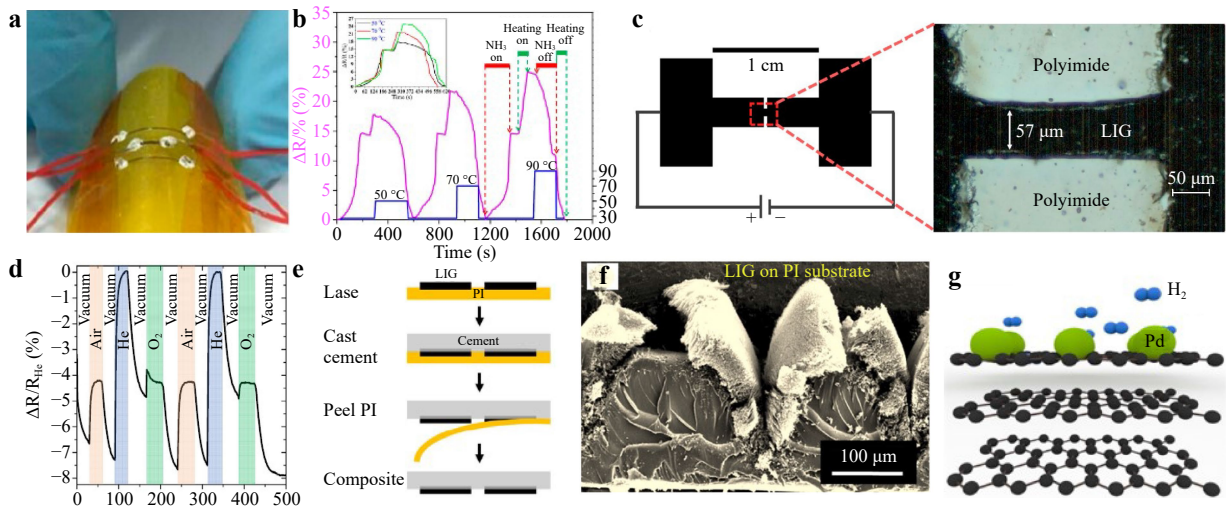

Fig. 14 a Photos of test samples of sensors[145]. **b** Normalized real-time resistance response/recovery behavior of sensor to 235 ppm NH_3 at 50~90 °C[145]. **c** Schematic diagram of gas sensor with LSG filament; all black parts represent LSG. Inset is an optical image of LSG filament 57-μm wide[146]. **d** Sensor responds to various gases at 12 V and shows repeatability. Shaded areas indicate sensor exposure to various gases[146]. **e** Schematic diagram shows process of embedding LSG-based sensors in cement; 50 μm active filament is not drawn[146]. **f** Cross-sectional SEM image of LSG structure[147]. **g** Schematic diagram of H_2 adsorption on LSG/Pd[147].

LSG as the electrode material with an LSG filament in the middle, where fluctuations in the thermal conductivity of the surrounding gas caused changes in the resistivity of the LSG filament. Therefore, this sensor had different sensitivities to different gases and can detect various gas mixtures, as shown in Fig. 14c, d. As shown in Fig. 14e, LSG sensors can be embedded in cement, which allows LSG-based gas detection in industrial or residential buildings. Although graphene is not sensitive to nonpolar gases such as hydrogen (H_2), Zhu et al. developed an LSG hydrogen sensor by mimicking the turbinate structures found in animal noses[147]. Fig. 14f shows the porous biomimetic turbinate-like LSG structure generated by the rapid release of the gaseous products. Owing to the catalytic effect of the Pd NPs on the crystal defects of the biomimetic turbinate-like microstructure, the adsorption and desorption of H_2 were more straightforward, as shown in Fig. 14g, where electrons were transferred to the defective holes of LSG, which leads the adsorption of H_2 on the Pd NPs to change the resistance and allow for H_2 detection.

Humidity sensors

The LSG-based humidity sensor has a higher linear response to humidity changes and more significant thermal stability than other functional conductive materials[148,149]. As shown in Fig. 15a, Cai et al. fabricated a humidity sensor using the laser cross-reduction of GO[150]. LSG was used as the conductive electrode of the humidity sensor and GO was used as the solid-state electrolyte. Fig. 15b shows that Cai et al. are the first to measure the output voltage wave in the alternating current (AC) detection mode instead of the conventional resistance, impedance, or capacitance. The sensitivity was significantly improved by approximately 45 times compared to the low and unstable responses in the direct current (DC) mode[150]. Interestingly, the humidity sensor can replace conventional large humidity measurement systems with a cell phone, as shown in Fig. 15c.

Li et al. employed LSG from a commercial DVD drive to fabricate an interdigital electrode (IDE), and then drop-casted a GO layer on the IDE as a sensing material[151]. The hydrophilic nature of GO promoted the absorption of water molecules, thereby enhancing its sensitivity. The sensitivity of the LSG-GO sensor was 4770.14 pF/% relative humidity (RH), which was more than ten times that of the LSG sensor (416.52 pF/% RH). Based on the hydrophilic nature of GO, Zhu et al. used a CO_2 laser to induce the generation of the IDE of LSG on a PI film, prepared as shown in Fig. 15d, and used GO as a sensitive layer[152]. Because the porous structure of LSG can increase the hydrophilic specific surface area of GO, both improved the performance of the humidity sensor.

As shown in Fig. 15e, the capacitive humidity-sensing mechanism was further investigated using impedance spectroscopy. The change in capacitance represents the number of adsorbed water molecules. However, at high RH, it was more difficult for the sensor to reach saturation, likely because of water molecules entering the GO interior.

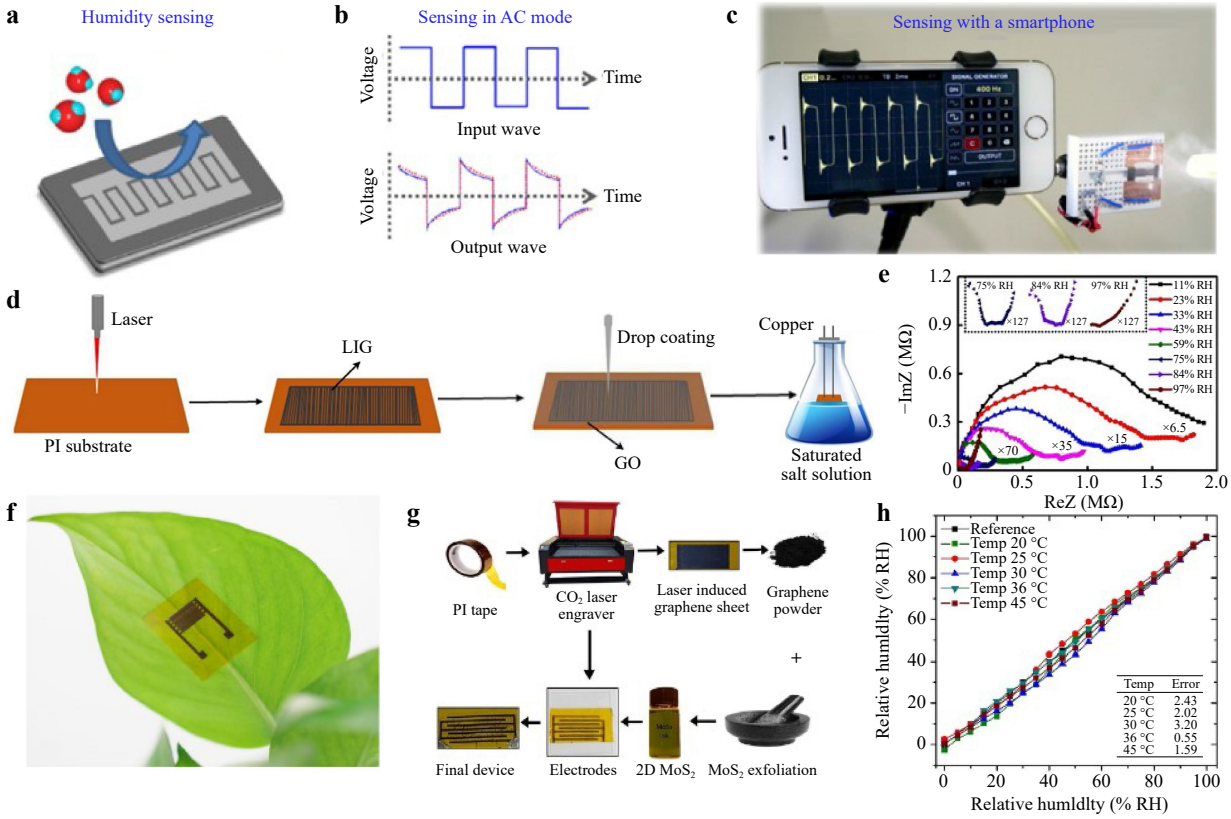

Fig. 15 a Schematic diagram of humidity sensor[150]. **b** Schematic diagram of applied AC voltage (top) and sensor output response (bottom)[150]. **c** Schematic diagram of measuring data using a smartphone[150]. **d** Schematic diagram of preparation process of humidity sensor[152]. **e** Complex impedance diagram at different RH levels; inset: enlarged curves of 75, 84, and 97% RH[152]. **f** Photo of LSG-based humidity sensor attached to lower surface of leaves[153]. **g** Step-by-step material synthesis and sensor manufacturing process. LSG electrode preparation and 2D nanocomposite solution demonstrated by mixing LSG powder and MoS_2 and then deposited on LSG electrode[154]. **h** Relative humidity error at different temperatures[154].

The sensor exhibited high performance from 11 to 97% RH and could effectively monitor humidity and respiration in a noncontact manner.

Lan et al. successfully applied an LSG/GO capacitive sensor to monitor plants, as shown in Fig. 15f, where the sensor was attached directly to plant leaves to track transpiration from stomata in real time over a time period without causing any damage to the plant[153]. Khattak et al. developed a humidity sensor that was not affected by temperature[154]. As shown in Fig. 15g, LSG was used as the sensor electrode. 2D graphene was extracted from LSG, and 2D graphene and MoS_2 were fabricated into a composite material that was used as the active layer. As the temperature increased, the mobility of MoS_2 decreased, whereas the conductivity of graphene increased; these opposite effects were effectively counteracted, resulting in a temperature-independent device. The sensor exhibited an excellent output response over the full range of 0–100% RH and excellent response and recovery times (4 s/2 s). Fig. 15h shows a minor error between the impedance curves obtained at different temperatures, indicating the temperature independence of the sensor. This allows the sensor to perform humidity measurements in environments with fluctuating temperatures.

Multifunctional sensors

Typical sensors can measure only one physical/biological signal and may not respond to other signals. The combination and measurement of multiple signals is necessary to enable more comprehensive and accurate applications in various fields[155,156]. However, the integration process is generally complex and reduces device accuracy. To solve this problem, multifunctional sensors that can measure multiple signals on a single sensor have been investigated[157,158]. Gao et al. reported a wearable multifunctional sweat detection LSG sensor integrated with uric acid (UA), tyrosine (Tyr), temperature, and strain sensors, as depicted in Fig. 16a, b[159]. Fig. 16c–f

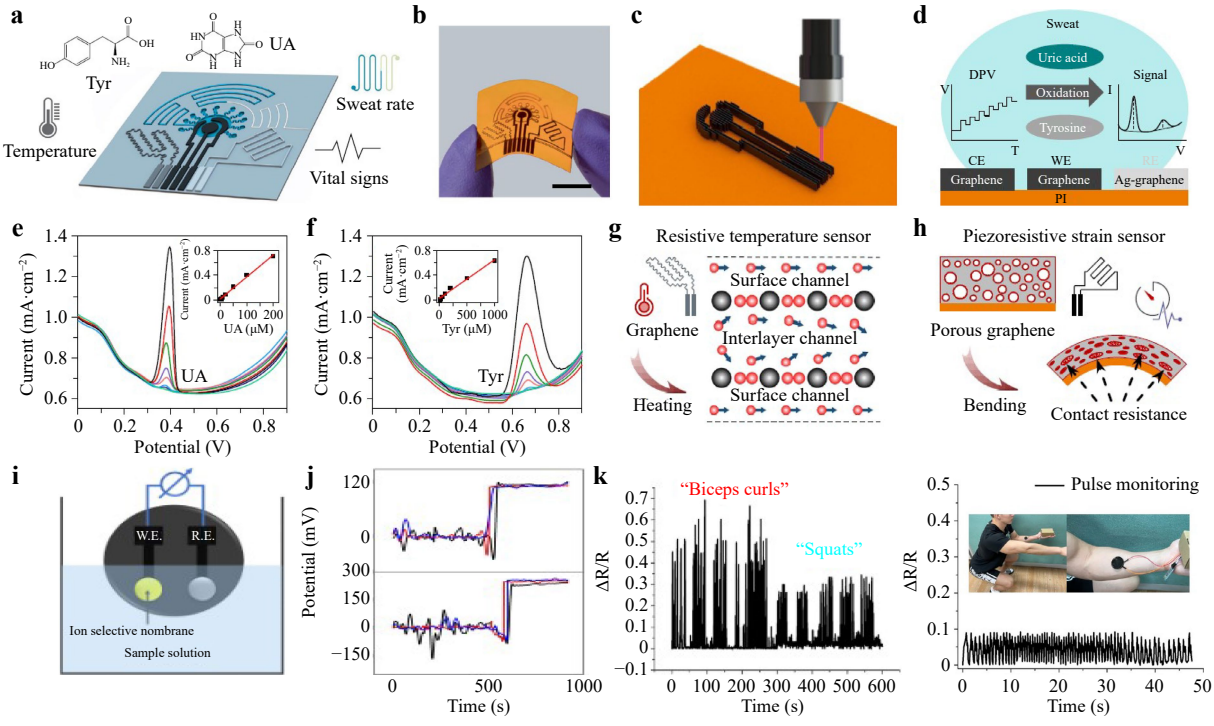

Fig. 16 a Multiple functions of sensor: ultra-sensitive sweat UA and Tyr detection, temperature sensing, and vital signs (for example, heart rate and respiratory rate) monitoring[159]. **b** Photos of flexible skin patches; scale bar of 1 cm[159]. **c** Schematic of raster mode for UA and Tyr sensor fabrication[159]. **d** Three-electrode LSG-based flexible sensor for simultaneous UA and Tyr detection[159]. UA **e** and Tyr **f** detection with LSG sensor in 0.01 M ABS solution; insets correspond to calibration diagram[159]. **g** Mechanism of LSG temperature sensing[159]. **h** Mechanism of LSG strain sensing[159]. **i** Schematic diagram of ion selective electrode principle[160]. **j** Monitoring sodium and potassium ions in sweat during weight-bearing training[160]. **k** Muscle contraction and pulse monitoring of multifunctional sensor patch during weight-bearing training[160].

show that the three-electrode LSG sensor can selectively catalyze the oxidation of UA and Tyr at specific potentials, enabling the detection of UA and Tyr in sweat associated with cardiovascular diseases, gout, metabolic disorders, and other diseases. As shown in Fig. 16g, h, for the temperature sensor, when the temperature increased, the electron-phonon scattering and electron thermal velocity in the interlayer increased its conductivity. The sensitivity of the sensor was −0.06% ℃$^{-1}$, with a low detection limit of 0.051 ℃. For the strain sensor, the external strain compressed the porous structure of the LSG, resulting in a decreased resistance. This fully LSG-based multifunctional sensor promotes scalability and flexibility, and demonstrates its potential for monitoring related diseases such as gout.

Lee et al. proposed a multifunctional sensor patch based on LSG that can simultaneously monitor the concentration of sodium and potassium ions in human sweat and strain generated by human movement[160]. As shown in Fig. 16i, the ion concentration was obtained by measuring the potential difference between the WE and RE. In addition, the sensor was sensitive to strain owing to the piezoresistive effect between the graphene layers. Fig. 16j, k shows the sensor patch applied to the skin of a volunteer, and the changes in the concentrations of the two ions in response to sweat during exercise were tested. As exercise time increased, the Na^+ and K^+ in sweat increased and dehydration started to occur. In addition, the pulse signal, during muscle contraction and relaxation monitoring when performing deep squats, demonstrates the promise of this multifunctional sensor for monitoring real-time vital signs.

For multifunctional sensors, reducing the crosstalk between various signals is critical. Chhetry et al. achieved temperature and pressure sensing capabilities by analyzing the independent thermoelectric and piezoresistive effects[161]. The sensor was designed with the geometry shown in Fig. 17a, where the stress was concentrated in the center when tension was applied, and the temperature-sensing mechanism was located at both ends, thus suppressing the strain in the temperature-sensing unit without affecting the performance of the strain sensing unit. As shown in Fig. 17b, c, the sensor exhibits a synthetic thermal index of 8,106 K in the range of 25–80 ℃ (temperature coefficient of resistance is 0.1736% ℃$^{-1}$) and high strain sensitivity of

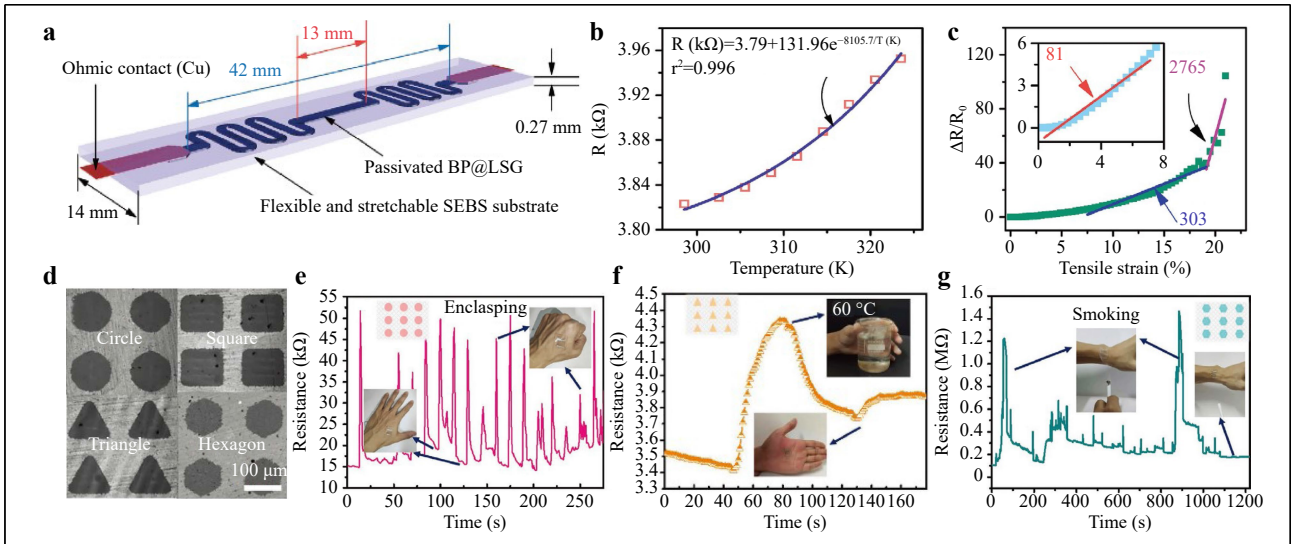

Fig. 17 **a** Schematic diagram of overall structure of multifunctional sensor[161]. **b** Schematic diagram of resistance response of passivated BP@LSG composites with temperature changes[161]. **c** Normalized value of resistance change with strain indicates strain sensitivity (i.e., GF)[161]. **d** Laser scribing optical image of graphene with 100-μm space [162]. **e** Stress sensor detects resistance to change with enclasping and unfolding of gestures[162]. **f** Resistance response to temperature[162]. **g** Resistance response to smoke[162].

up to 2,765 (> 19.2%), enabling the measurement of human body temperature and monitoring of various deformations caused by the human body. Interestingly, Ye et al. prepared four graphene arrays—circular, square, triangular, and hexagonal—by the local ablation of graphene films using a femtosecond laser, as shown in Fig. 17d[162]. Differently patterned graphene exhibited significant sensing selectivity owing to the overhanging bonds and empty sites at the edges of the patterns. The sensitivity of the sensor was evaluated by recording the change in resistance. Fig. 17e–g shows that the sensor simultaneously detects the human pulse, temperature, and harmful gases and can be applied to the human body or clothing to provide real-time health monitoring and protection.

Conclusion and prospect

In this paper, we summarized the latest research on LSG sensor applications. First, we discussed the preparation and modification of LSG using different laser light sources and precursors, including various carbon precursors, such as GO and polymer. Conventional graphene preparation methods are energy-intensive, costly, or environment-unfriendly, but the laser scribing method for graphene preparation overcomes these drawbacks. LSG can be modified in one step by adjusting the laser parameters, atmosphere, and doping. The large surface area, good electrical conductivity, and simple and efficient fabrication process of LSG make it an excellent candidate for sensor applications. This paper summarized the applications of LSG in stress, bio, gas, temperature, and humidity sensors. The performance of the sensors can be optimized using the appropriate laser power, scan speed, scan spacing, and suitable doping of LSG during LSG preparation. LSG sensors with multiple integrated sensing functions were introduced. For multifunctional sensors, the crosstalk between different signals can be reduced by structural design and patterning. Table 1 summarizes the performances and applications of LSG-based sensors. In particular, the flexible patterned preparation and various flexible substrates make LSG promising for wearable sensor applications.

Although LSG-based sensors have been proven to have many advantages, there still remain challenges and room for further development. New precursors for LSG preparation can be further explored to investigate different possible properties of LSG and further enhance the large-scale preparation of LSG. In addition, the adhesion ability of LSG on PI is weak, which is a significant challenge for flexible sensors[30]. Therefore, the exploration of new precursors that can further improve the efficiency of LSG sensor fabrication is required. Meanwhile, LSG produces many defects compared with other graphene preparation methods. These defects may affect the LSG performance. Therefore, further in-depth studies on the principles and mechanisms of the defects are required. For example, Li et al. and Banerjee et al. demonstrated that defects in graphene greatly enhance the electron transfer kinetics at edge positions[163,164], which are crucial for the performance of the sensor.

Sensitivity and sensing range are two critical factors in

Table 1 Review of the performance of LSG-based sensors.

Materials	Analytes	Sensitivity/GF	Response/Recovery	Comments	Ref
LSG/PU, PS	Pressure	149 kPa^{-1} (0–1 kPa) 659 kPa^{-1} (1–10 kPa) 2048 kPa^{-1} (10–100 kPa)	–	Self-healing, flexible, and highly sensitive pressure.	2
MoS_2/LSG	Strain	236.2 (0–16.7%) 1242 (16.7–25%)	0.25 s/0.17 s	-Able to detect fine deformation. - Highly sensitive, reliable, and hysteresis-free.	3
LSG, PDMS	Pressure	2.2 kPa^{-1} (0–1 kPa)	< 50 ms/< 50 ms	Highly conductive graphitic structures produced by irradiating defocused fs laser pulses under ambient conditions.	80
LSG/PS	Strain	250 (0–1.05%) 725 (1.05–3.5%)	< 100 ms	Ultra-sensitive small strain detection.	87
LSG/Au NPs	Strain	52.5 (0–25.4%)	–	Improved carrier mobility of LSG.	85
LSG/Pt NPs	Strain	45.6 (0–6%) 269.5 (6–16%) 489.3 (16–20%)	–	Low hysteresis, minor lag errors, and highly stable response (> 5000 cycles).	86
LSG, PDMS	Pressure	0.011 kPa^{-1} (0–15 kPa) 0.026 kPa^{-1} (15–40 kPa) 0.004 kPa^{-1} (40–100 kPa)	120 ms/150 ms	Ability to distinguish between different external mechanical stimuli by multiple responses, avoiding signal conflicts.	103
LSG/MXene	Pressure	2.25 kPa^{-1} (0–200 Pa)	0.144 s/0.144 s	High sensitivity, ultra-low detection limit, rapid response, and extreme durability.	106
LSG/MWCNTs	Pressure	2.41 kPa^{-1} (0–200 Pa)	2 ms/2 ms	Resistance sensitivity improved by the synergistic interaction between graphene nanosheets and MWCNTs.	107
LSG, PDMS, ITO/PET	Pressure	7.697 kPa^{-1} (< 1 kPa) 0.938 kPa^{-1} (1–20 kPa) 0.136 kPa^{-1} (> 20 kPa)	9.9 ms/–	Flexible, self-powered, and inexpensive	109
LSG/MWCNT-AuNPs	Nitrite	0.9 μM (10–140 μM)	–	Sensitive, selective, and reproducible	116
LSG/ISEs	K^+ NH_4^+	53 mV^{-1} (3×10^{-4}–150×10^{-3} M) 51 mV^{-1} (1×10^{-4}–150×10^{-3} M)	30 s/–	High stability (minimal drop in signal over 3 months of storage) across a wide range of pH (3.5–9.0).	117
LSG/Ni/Au	Glucose	3500 μA mM^{-1} cm^{-2} (0–4 mM)	<1 s/–	-Wearable with sweat sampling capability. -Porous Ecoflex package promotes diffusion of sampling solution and reduces evaporation, resulting in faster and more accurate measurements.	124
LSG/PEDOT	Dopamine	0.220±0.011 μA μM^{-1} (1–150 μM)	–	Sensitive, selective, and disposable electrochemical dopamine sensor.	126
LSG/Ag NPs	H_2O_2	7.9 μM (0.1–10 mM)	3 s/–	Suitable for the development of sensitivity, selective, and integrated electrochemical systems.	128
LSG/N	miRNA	10 fM-10 nM	–	- N-doped porous graphene with improved conductivity and sensitivity to miRNA. -Easy fabrication, low cost, and high performance	130
LSG/$ZnFe_2O_4$	cTn-I	19.32 (± 0.25) μA/(ng/mL) (0.001–200 ng/mL)	–	Higher selectivity towards cTn-I detedtion	134
LSG/ AuNPs-Apt/ MB	Insulin	22.7 fM (0.1 pM–0.1 μM)	–	Single-use and highly sensitive	136
LSG	Temperature	0.37% $°C^{-1}$ (30–100 °C)	0.196 s/9.7 s	Fast response time, good linearity, small hysteresis, good repeatability, and stable performance	141
LSG, PCB	Temperature	13.1% (–10 °C–50 °C)	–	Simple integration and real-time performance of temperature detection data.	142
LSG	NH_3	0.087% ppm^{-1} (75 ppm–400 ppm)	214 s/222 s	One-step process and free of additional assemblies.	145

TABLE 1 (continued)

Materials	Analytes	Sensitivity/GF	Response/Recovery	Comments	Ref
LSG, GO	Humidity	9150 pF/%RH (11–97%RH)	49 s/2 s	High sensitivity, stability, reliability, and short response/recovery time.	152
LSG/MoS_2	Humidity	8% (0–50%RH) 80% (50–100%RH)	4 s/2 s	Humidity measurement can be performed in environments with fluctuating temperatures.	154
LSG	UA Tyr Temperature Strain	3.50 μA $μM^{-1}$ cm^{-2} 0.61 μA $μM^{-1}$ cm^{-2} −0.06% $°C^{-1}$ –	–	- Highly efficient microfluidic sweat sampling, sensitive molecular sensing, and multiple vital sign sensing. - Fast electron mobility, high current density, and ultra-large surface area.	159
LSG, PDMS/lignin	Na^+ K+ Strain	59.2 mV/dec (10^{-7}–10^{-1} M) 59.2 mV/dec (10^{-8}–10^{-1} M) 20	–	Real-time vital sign monitoring by monitoring sodium and potassium levels and pulse rate in sweat.	160
LSG/BP, SEBS	Strain Temperature	81.2 (0–7.5%) 302.7 (7.5–19.2%) 2765 (> 19.2%) 8106 K (25–50 °C)	–	Unique hybridized sensor design enables efficient and accurate determination of each parameter.	161
LSG	Strain Temperature CO	496.7 (1–10%) 139 (35–42 °C) $6.68×10^4$ (100–1000 ppm)	–	Significant selectivity of different model arrays for different environmental changes.	162

sensor performance for stress sensors. However, it is difficult for stress sensors to have both high sensitivity and a wide detection range. New techniques can be explored to solve this problem, such as designing suitable graphene surface microstructures and doping to enhance the comprehensive performance. Recently, Wu et al. reported a stress sensor with a positive correlation between the resistance change and external force to improve the sensitivity and sensing range of the sensor[165]. Most published stress sensors have a negative correlation between resistance change and external force, which limits the range of resistance change to 100%; thus, limiting the sensing range. Therefore, attempting to positively correlating the change in resistance with the external force is a worthwhile endeavor.

Electrochemical tests can be used to analyze biosensors; thus, more analytical methods can be explored. Moreover, in biosensors, LSG is used as the working electrode for direct electrochemical testing; therefore, the properties of LSG can be exploited to study suitable doping substances to improve the charge transfer rate of the LSG WE, and thus improve sensitivity. In addition, in terms of laser type, ultrafine laser lithography can maximize the specific surface area of graphene structures, leading to performance breakthroughs, which is an essential research direction for the future[166].

We expect that the integration of LSG sensors with other LSG devices, such as nanogenerators and supercapacitors, will be explored to provide and store energy. The integration of LSG sensors with artificial intelligence techniques, including intelligent graphics, can also be explored to design LSGs with improved sensor performance. Finally, LSG-based sensors can be applied to robotics, enabling them to monitor external data in real time.

Acknowledgements

The authors acknowledge funding support from the Science and Technology Commission of Shanghai Municipality (Grant No. 21DZ1100500), Shanghai Municipal Science and Technology Major Project, and Shanghai Frontiers Science Center Program (2021-2025 No. 20). Fangyi Zhang acknowledges the continued support from the Queensland University of Technology (QUT) through the Centre for Robotics. Zhengfen Wan thanks the National Natural Science Foundation of China (Grant No. 62105206) and the China Postdoctoral Science Foundation (No. 2021M692137) for their support. Xi Chen acknowledges the support from the National Natural Science Foundation of China (Grant No. 11974247).

Author details

[1]Institute of Photonic Chips, University of Shanghai for Science and Technology, Shanghai 200093, China. [2]Centre for Artificial-Intelligence Nanophotonics, School of Optical-Electrical and Computer Engineering, University of Shanghai for Science and Technology, Shanghai 200093, China. [3]Queensland University of Technology (QUT) Centre for Robotics, Brisbane, QLD 4000, Australia

Conflict of interest

The authors declare no conflicts of interest.

Received: 28 October 2022 Revised: 17 April 2023 Accepted: 18 April 2023
Accepted article preview online: 20 April 2023
Published online: 05 June 2023

References

1. Wang, H. et al. Laser-induced graphene based flexible electronic devices. *Biosensors* **12**, 55 (2022).

2. Tian, Q. et al. Bean pod-inspired ultrasensitive and self-healing pressure sensor based on laser-induced graphene and polystyrene microsphere sandwiched structure. *ACS Applied Materials & Interfaces* **12**, 9710-9717 (2020).
3. Chhetry, A. et al. MoS_2-decorated laser-induced graphene for a highly sensitive, hysteresis-free, and reliable piezoresistive strain sensor. *ACS Applied Materials & Interfaces* **11**, 22531-22542 (2019).
4. Lu, Z. W. et al. Novel flexible bifunctional amperometric biosensor based on laser engraved porous graphene array electrodes: highly sensitive electrochemical determination of hydrogen peroxide and glucose. *Journal of Hazardous Materials* **402**, 123774 (2021).
5. Hui, X. et al. A highly flexible and selective dopamine sensor based on Pt-Au nanoparticle-modified laser-induced graphene. *Electrochimica Acta* **328**, 135066 (2019).
6. Gao, L. et al. Highly sensitive detection for proteins using graphene oxide-aptamer based sensors. *Nanoscale* **7**, 10903-10907 (2015).
7. Lin, X. N. et al. Laser engraved nitrogen-doped graphene sensor for the simultaneous determination of Cd(II) and Pb(II). *Journal of Electroanalytical Chemistry* **828**, 41-49 (2018).
8. Johnson, Z. T. et al. Electrochemical sensing of neonicotinoids using laser-induced graphene. *ACS Sensors* **6**, 3063-3071 (2021).
9. Yan, W. H. et al. Size-tunable flowerlike MoS_2 nanospheres combined with laser-induced graphene electrodes for NO_2 sensing. *ACS Applied Nano Materials* **3**, 2545-2553 (2020).
10. Silipigni, L. et al. Temperature sensor based on IR-laser reduced graphene oxide. *Journal of Instrumentation* **15**, C04006 (2020).
11. Hou, M. X. et al. Laser-induced graphene coated hollow-core fiber for humidity sensing. *Sensors and Actuators B:Chemical* **359**, 131530 (2022).
12. Novoselov, K. S. et al. Electric field effect in atomically thin carbon films. *Science* **306**, 666-669 (2004).
13. Li, X. S. et al. Large-area synthesis of high-quality and uniform graphene films on copper foils. *Science* **324**, 1312-1314 (2009).
14. Bae, S. et al. Roll-to-roll production of 30-inch graphene films for transparent electrodes. *Nature Nanotechnology* **5**, 574-578 (2010).
15. Real, M. A. et al. Graphene epitaxial growth on SiC(0001) for resistance standards. *IEEE Transactions on Instrumentation and Measurement* **62**, 1454-1460 (2013).
16. Wang, S. J. et al. Fabrication of highly conducting and transparent graphene films. *Carbon* **48**, 1815-1823 (2010).
17. Chua, C. K. & Pumera, M. Chemical reduction of graphene oxide: a synthetic chemistry viewpoint. *Chemical Society Reviews* **43**, 291-312 (2014).
18. Perumal, S., Atchudan, R. & Cheong, I. W. Recent studies on dispersion of graphene-polymer composites. *Polymers* **13**, 2375 (2021).
19. Yi, K. Y. et al. Plasma-enhanced chemical vapor deposition of two-dimensional materials for applications. *Accounts of Chemical Research* **54**, 1011-1022 (2021).
20. Yang, Z. Y. et al. A new direct growth method of graphene on Si-face of 6H-SiC by synergy of the inner and external carbon sources. *Applied Surface Science* **436**, 511-518 (2018).
21. Peng, L. et al. An iron-based green approach to 1-h production of single-layer graphene oxide. *Nature Communications* **6**, 5716 (2015).
22. Bergsman, D. S. et al. Preserving nanoscale features in polymers during laser induced graphene formation using sequential infiltration synthesis. *Nature Communications* **11**, 3636 (2020).
23. Guo, L. et al. Two-beam-laser interference mediated reduction, patterning and nanostructuring of graphene oxide for the production of a flexible humidity sensing device. *Carbon* **50**, 1667-1673 (2012).
24. Kang, S. M. et al. Roll-to-roll laser-printed graphene-graphitic carbon electrodes for high-performance supercapacitors. *ACS Applied Materials & Interfaces* **10**, 1033-1038 (2018).
25. Xu, Y. D. et al. Laser-induced graphene for bioelectronics and soft actuators. *Nano Research* **14**, 3033-3050 (2021).
26. Yin, K. et al. Solar-driven thermal-wind synergistic effect on laser-textured superhydrophilic copper foam architectures for ultrahigh efficient vapor generation. *Applied Physics Letters* **118**, 211905 (2021).
27. Wan, Z. F. et al. Laser-reduced graphene: synthesis, properties, and applications. *Advanced Materials Technologies* **3**, 1700315 (2018).
28. Ye, R. Q., James, D. K. & Tour, J. M. Laser-induced graphene: from discovery to translation. *Advanced Materials* **31**, 1803621 (2019).
29. Qu, M. L. et al. Whole-device mass-producible perovskite photodetector based on laser-induced graphene electrodes. *Advanced Optical Materials* **10**, 2201741 (2022).
30. Hong, J. L. et al. Transferred laser-scribed graphene-based durable and permeable strain sensor. *Advanced Materials Interfaces* **8**, 2100625 (2021).
31. Dosi, M. et al. Ultrasensitive electrochemical methane sensors based on solid polymer electrolyte-infused laser-induced graphene. *ACS Applied Materials & Interfaces* **11**, 6166-6173 (2019).
32. Santos, N. F. et al. IR and UV laser-induced graphene: application as dopamine electrochemical sensors. *Advanced Materials Technologies* **6**, 2100007 (2021).
33. Wang, F. C. et al. Laser-induced nitrogen-doped hierarchically porous graphene for advanced electrochemical energy storage. *Carbon* **150**, 396-407 (2019).
34. Kavinkumar, T. et al. High performance flexible solid-state symmetric supercapacitors based on laser induced porous reduced graphene oxide-graphene oxide hybrid nanostructure devices. *Applied Surface Science* **480**, 671-679 (2019).
35. Lamon, S. et al. Nanoscale optical writing through upconversion resonance energy transfer. *Science Advances* **7**, eabe2209 (2021).
36. Chen, X., Luan, H. T. & Gu, M. Beyond high-voltage capacitors: supercapacitor arrays based on laser-scribed subwavelength-featured graphene patterns. *ACS Applied Energy Materials* **5**, 9315-9323 (2022).
37. Chen, M. et al. Direct laser writing of graphene oxide for ultra-low power consumption memristors in reservoir computing for digital recognition. *National Science Open* **1**, 20220020 (2022).
38. Li, X. P. et al. Athermally photoreduced graphene oxides for three-dimensional holographic images. *Nature Communications* **6**, 6984 (2015).
39. Singh, S. P. et al. Laser-induced graphene layers and electrodes prevents microbial fouling and exerts antimicrobial action. *ACS Applied Materials & Interfaces* **9**, 18238-18247 (2017).
40. Stanford, M. G. et al. Self-sterilizing laser-induced graphene bacterial air filter. *ACS Nano* **13**, 11912-11920 (2019).
41. Li, R. Z. et al. Laser-scribed lossy microstrip lines for radio frequency applications. *Applied Sciences* **9**, 415 (2019).
42. Tkachev, S. V. et al. Reduced graphene oxide. *Inorganic Materials* **48**, 796-802 (2012).
43. Guan, Y. C. et al. Fabrication of laser-reduced graphene oxide in liquid nitrogen environment. *Scientific Reports* **6**, 28913 (2016).
44. Wang, S. C. et al. Diffractive photonic applications mediated by laser reduced graphene oxides. *Opto-Electronic Advances* **1**, 170002 (2018).
45. Ma, B. et al. The correlation between electrical conductivity and second-order Raman modes of laser-reduced graphene oxide. *Physical Chemistry Chemical Physics* **21**, 10125-10134 (2019).
46. Li, L. et al. High-performance pseudocapacitive microsupercapacitors from laser-induced graphene. *Advanced Materials* **28**, 838-845 (2016).

47. Tao, L. Q. et al. An intelligent artificial throat with sound-sensing ability based on laser induced graphene. *Nature Communications* **8**, 14579 (2017).
48. Duy, L. X. et al. Laser-induced graphene fibers. *Carbon* **126**, 472-479 (2018).
49. Kulyk, B. et al. Laser-induced graphene from paper for mechanical sensing. *ACS Applied Materials & Interfaces* **13**, 10210-10221 (2021).
50. Wan, Z. F., Chen, X. & Gu, M. Laser scribed graphene for supercapacitors. *Opto-Electronic Advances* **4**, 200079 (2021).
51. Le, T. S. D. et al. Ultrafast laser pulses enable one-step graphene patterning on woods and leaves for green electronics. *Advanced Functional Materials* **29**, 1902771 (2019).
52. Le, T. S. D. et al. Green flexible graphene-inorganic-hybrid micro-supercapacitors made of fallen leaves enabled by ultrafast laser pulses. *Advanced Functional Materials* **32**, 2107768 (2022).
53. Le, T. S. D. et al. Recent advances in laser-induced graphene: mechanism, fabrication, properties, and applications in flexible electronics. *Advanced Functional Materials* **32**, 2270276 (2022).
54. Rahimi, R. et al. Highly stretchable and sensitive unidirectional strain sensor via laser carbonization. *ACS Applied Materials & Interfaces* **7**, 4463-4470 (2015).
55. Carvalho, A. F. et al. Laser-induced graphene strain sensors produced by ultraviolet irradiation of polyimide. *Advanced Functional Materials* **28**, 1805271 (2018).
56. Cai, J. G., Lv, C. & Watanabe, A. Laser direct writing and selective metallization of metallic circuits for integrated wireless devices. *ACS Applied Materials & Interfaces* **10**, 915-924 (2018).
57. Kaidarova, A. & Kosel, J. Physical sensors based on laser-induced graphene: a review. *IEEE Sensors Journal* **21**, 12426-12443 (2021).
58. Chen, Y. et al. UV laser-induced polyimide-to-graphene conversion: modeling, fabrication, and application. *Small Methods* **3**, 1900280 (2019).
59. Peng, Z. W. et al. Flexible and stackable laser-induced graphene supercapacitors. *ACS Applied Materials & Interfaces* **7**, 3414-3419 (2015).
60. Stanford, M. G. et al. High-resolution laser-induced graphene. *flexible electronics beyond the visible limit. ACS Applied Materials & Interfaces* **12**, 10902-10907 (2020).
61. Zhang, Y. L. et al. Direct imprinting of microcircuits on graphene oxides film by femtosecond laser reduction. *Nano Today* **5**, 15-20 (2010).
62. Hyeong, S. K. et al. Review of the direct laser synthesis of functionalized graphene and its application in sensor technology. *Applied Science and Convergence Technology* **28**, 148-154 (2019).
63. Wan, Z. F. et al. Tuning the sub-processes in laser reduction of graphene oxide by adjusting the power and scanning speed of laser. *Carbon* **141**, 83-91 (2019).
64. Huang, L. et al. Pulsed laser assisted reduction of graphene oxide. *Carbon* **49**, 2431-2436 (2011).
65. Hu, Y. et al. All-in-one graphene fiber supercapacitor. *Nanoscale* **6**, 6448-6451 (2014).
66. Cheng, H. H. et al. A general and extremely simple remote approach toward graphene bulks with in situ multifunctionalization. *Advanced Materials* **28**, 3305-3312 (2016).
67. Lin, J. et al. Laser-induced porous graphene films from commercial polymers. *Nature Communications* **5**, 5714 (2014).
68. Wan, Z. F. et al. Laser induced graphene for biosensors. *Sustainable Materials and Technologies* **25**, e00205 (2020).
69. Carvalho, A. F. et al. Laser-induced graphene piezoresistive sensors synthesized directly on cork insoles for gait analysis. *Advanced Materials Technologies* **5**, 2000630 (2020).
70. Zhang, N., Yang, J. & Hu, C. G. Laser-scribed graphene sensors on nail polish with tunable composition for electrochemical detection of nitrite and glucose. *Sensors and Actuators B:Chemical* **357**, 131394 (2022).
71. Kulyk, B. et al. Conversion of paper and xylan into laser-induced graphene for environmentally friendly sensors. *Diamond and Related Materials* **123**, 108855 (2022).
72. Ye, R. Q. et al. Laser-induced graphene formation on wood. *Advanced Materials* **29**, 1702211 (2017).
73. Kulyk, B. et al. Laser-induced graphene from paper by ultraviolet irradiation: humidity and temperature sensors. *Advanced Materials Technologies* **7**, 2101311 (2022).
74. Lei, Y. J. et al. Laser-scribed graphene electrodes derived from lignin for biochemical sensing. *ACS Applied Nano Materials* **3**, 1166-1174 (2020).
75. Chyan, Y. et al. Laser-induced graphene by multiple lasing: toward electronics on cloth, paper, and food. *ACS Nano* **12**, 2176-2183 (2018).
76. Zhang, Z. C. et al. Visible light laser-induced graphene from phenolic resin: a new approach for directly writing graphene-based electrochemical devices on various substrates. *Carbon* **127**, 287-296 (2018).
77. Zhu, Y. S. et al. Fabrication of low-cost and highly sensitive graphene-based pressure sensors by direct laser scribing polydimethylsiloxane. *ACS Applied Materials & Interfaces* **11**, 6195-6200 (2019).
78. Lamberti, A. et al. New insights on laser-induced graphene electrodes for flexible supercapacitors: tunable morphology and physical properties. *Nanotechnology* **28**, 174002 (2017).
79. Liu, H. L. et al. Effect of pulsed Nd: YAG laser processing parameters on surface properties of polyimide films. *Surface and Coatings Technology* **361**, 102-111 (2019).
80. Hayashi, S., Morosawa, F. & Terakawa, M. Laser direct writing of highly crystalline graphene on polydimethylsiloxane for fingertip-sized piezoelectric sensors. *Advanced Engineering Materials* **23**, 2100457 (2021).
81. Li, Y. L. et al. Laser-induced graphene in controlled atmospheres: from superhydrophilic to superhydrophobic surfaces. *Advanced Materials* **29**, 1700496 (2017).
82. Choudhury, S. et al. Potentiometric ion-selective sensors based on UV-ozone irradiated laser-induced graphene electrode. *Electrochimica Acta* **387**, 138341 (2021).
83. Feng, J. & Guo, Z. G. Wettability of graphene: from influencing factors and reversible conversions to potential applications. *Nanoscale Horizons* **4**, 339-364 (2019).
84. Zhu, J. B., Huang, X. & Song, W. X. Physical and chemical sensors on the basis of laser-induced graphene: mechanisms, applications, and perspectives. *ACS Nano* **15**, 18708-18741 (2021).
85. Wan, Z. F. et al. Localized surface plasmon enhanced laser reduction of graphene oxide for wearable strain sensor. *Advanced Materials Technologies* **6**, 2001191 (2021).
86. Liu, W. et al. In situ laser synthesis of Pt nanoparticles embedded in graphene films for wearable strain sensors with ultra-high sensitivity and stability. *Carbon* **190**, 245-254 (2022).
87. Gong, T. X. et al. Highly responsive flexible strain sensor using polystyrene nanoparticle doped reduced graphene oxide for human health monitoring. *Carbon* **140**, 286-295 (2018).
88. Tehrani, F. & Bavarian, B. Facile and scalable disposable sensor based on laser engraved graphene for electrochemical detection of glucose. *Scientific Reports* **6**, 27975 (2016).
89. Meng, L. Y., Turner, A. P. F. & Mak, W. C. Conducting polymer-reinforced laser-irradiated graphene as a heterostructured 3D transducer for flexible skin patch biosensors. *ACS Applied Materials & Interfaces* **13**, 54456-54465 (2021).

90. Prabhakaran, A. & Nayak, P. Surface engineering of laser-scribed graphene sensor enables non-enzymatic glucose detection in human body fluids. *ACS Applied Nano Materials* **3**, 391-398 (2020).
91. Qiu, D. Y. et al. A low-cost wireless intelligent portable sensor based on disposable laser-induced porous graphene flexible electrode decorated by gold nanoshells for rapid detection of sulfonamides in aquatic products. *Food Analytical Methods* **15**, 1471-1481 (2022).
92. Mao, L. N. et al. Morphologically modulated laser-patterned reduced graphene oxide strain sensors for human fatigue recognition. *Smart Materials and Structures* **29**, 015009 (2020).
93. Wei, S. et al. Flexible large e-skin array based on patterned laser-induced graphene for tactile perception. *Sensors and Actuators A:Physical* **334**, 113308 (2022).
94. Iqra, M. et al. A flexible piezoresistive strain sensor based on laser scribed graphene oxide on polydimethylsiloxane. *Scientific Reports* **12**, 4882 (2022).
95. Liu, W. et al. Stable wearable strain sensors on textiles by direct laser writing of graphene. *ACS Applied Nano Materials* **3**, 283-293 (2020).
96. Zhao, C. et al. A novel micro-pressure graphene sensor array with double-layer mesh structure. *IEEE Sensors Journal* **22**, 1964-1971 (2022).
97. Jeong, S. Y. et al. Highly skin-conformal laser-induced graphene-based human motion monitoring sensor. *Nanomaterials* **11**, 951 (2021).
98. Duan, S. S. et al. Waterproof mechanically robust multifunctional conformal sensors for underwater interactive human-machine interfaces. *Advanced Intelligent Systems* **3**, 2100056 (2021).
99. Hao, D. P. et al. Highly sensitive piezoresistive pressure sensors based on laser-induced graphene with molybdenum disulfide nanoparticles. *Science China Technological Sciences* **64**, 2408-2414 (2021).
100. Shrestha, K. et al. A siloxene/ecoflex nanocomposite-based triboelectric nanogenerator with enhanced charge retention by MoS_2/LIG for self-powered touchless sensor applications. *Advanced Functional Materials* **32**, 2270155 (2022).
101. Cao, H. et al. Development and characterization of a novel interdigitated capacitive strain sensor for structural health monitoring. *IEEE Sensors Journal* **15**, 6542-6548 (2015).
102. Han, T. et al. Multifunctional flexible sensor based on laser-induced graphene. *Sensors* **19**, 3477 (2019).
103. Huang, L. X. et al. Flexible capacitive pressure sensor based on laser-induced graphene and polydimethylsiloxane foam. *IEEE Sensors Journal* **21**, 12048-12056 (2021).
104. Zhu, Y. S. et al. Highly sensitive and skin-like pressure sensor based on asymmetric double-layered structures of reduced graphite oxide. *Sensors and Actuators B:Chemical* **255**, 1262-1267 (2018).
105. Zhao, J. et al. Highly responsive screen-printed asymmetric pressure sensor based on laser-induced graphene. *Journal of Micromechanics and Microengineering* **32**, 015002 (2022).
106. Zhao, J. et al. Highly responsive asymmetric pressure sensor based on MXene/reduced graphene oxide nanocomposite fabricated by laser scribing technique. *IEEE Sensors Journal* **21**, 26673-26680 (2021).
107. Zhao, J. et al. Novel multi-walled carbon nanotubes-embedded laser-induced graphene in crosslinked architecture for highly responsive asymmetric pressure sensor. *Sensors and Actuators A:Physical* **323**, 112658 (2021).
108. Xia, S. Y. et al. Laser-induced graphene (LIG)-based pressure sensor and triboelectric nanogenerator towards high-performance self-powered measurement-control combined system. *Nano Energy* **96**, 107099 (2022).
109. Das, P. S. et al. A laser ablated graphene-based flexible self-powered pressure sensor for human gestures and finger pulse monitoring. *Nano Research* **12**, 1789-1795 (2019).
110. Yan, Z. G. et al. Flexible high-resolution triboelectric sensor array based on patterned laser-induced graphene for self-powered real-time tactile sensing. *Advanced Functional Materials* **31**, 2100709 (2021).
111. Soares, R. R. A. et al. Laser-induced graphene electrochemical immunosensors for rapid and label-free monitoring of salmonella enterica in chicken broth. *ACS Sensors* **5**, 1900-1911 (2020).
112. Nasraoui, S. et al. Development of an efficient voltammetric sensor for the monitoring of 4-aminophenol based on flexible laser induced graphene electrodes modified with MWCNT-PANI. *Sensors* **22**, 833 (2022).
113. Chang, Z. et al. Electrochemical aptasensor for 17β-estradiol using disposable laser scribed graphene electrodes. *Biosensors and Bioelectronics* **185**, 113247 (2021).
114. Ge, L. et al. Direct-laser-writing of metal sulfide-graphene nanocomposite photoelectrode toward sensitive photoelectrochemical sensing. *Advanced Functional Materials* **29**, 1904000 (2019).
115. Garland, N. T. et al. Flexible laser-induced graphene for nitrogen sensing in soil. *ACS Applied Materials & Interfaces* **10**, 39124-39133 (2018).
116. Nasraoui, S. et al. Electrochemical sensor for nitrite detection in water samples using flexible laser-induced graphene electrodes functionalized by CNT decorated by Au nanoparticles. *Journal of Electroanalytical Chemistry* **880**, 114893 (2021).
117. Kucherenko, I. S. et al. Ion-selective sensors based on laser-induced graphene for evaluating human hydration levels using urine samples. *Advanced Materials Technologies* **5**, 1901037 (2020).
118. Zhao, J. et al. Co_3O_4 nanoparticles embedded in laser-induced graphene for a flexible and highly sensitive enzyme-free glucose biosensor. *Sensors and Actuators B:Chemical* **347**, 130653 (2021).
119. Zhang, Y. et al. A flexible non-enzymatic glucose sensor based on copper nanoparticles anchored on laser-induced graphene. *Carbon* **156**, 506-513 (2020).
120. Settu, K., Lai, Y. C. & Liao, C. T. Carbon nanotube modified laser-induced graphene electrode for hydrogen peroxide sensing. *Materials Letters* **300**, 130106 (2021).
121. Matias, T. A. et al. Prussian blue-modified laser-induced graphene platforms for detection of hydrogen peroxide. *Microchimica Acta* **189**, 188 (2022).
122. Settu, K., Chiu, P. T. & Huang, Y. M. Laser-Induced Graphene-Based Enzymatic Biosensor for Glucose Detection. *Polymers* **13**, 2795 (2021).
123. Yoon, H. et al. A chemically modified laser-induced porous graphene based flexible and ultrasensitive electrochemical biosensor for sweat glucose detection. *Sensors and Actuators B:Chemical* **311**, 127866 (2020).
124. Zhu, J. et al. Laser-induced graphene non-enzymatic glucose sensors for on-body measurements. *Biosensors and Bioelectronics* **193**, 113606 (2021).
125. Shang, N. G. et al. Catalyst-free efficient growth, orientation and biosensing properties of multilayer graphene nanoflake films with sharp edge planes. *Advanced Functional Materials* **18**, 3506-3514 (2008).
126. Xu, G. Y. et al. Sensitive, selective, disposable electrochemical dopamine sensor based on PEDOT-modified laser scribed graphene. *Biosensors and Bioelectronics* **107**, 184-191 (2018).
127. Chen, W. et al. Recent advances in electrochemical sensing for hydrogen peroxide: a review. *Analyst* **137**, 49-58 (2012).
128. Aparicio-Martínez, E. et al. Flexible electrochemical sensor based on laser scribed Graphene/Ag nanoparticles for non-enzymatic

hydrogen peroxide detection. *Sensors and Actuators B:Chemical* **301**, 127101 (2019).
129. Yagati, A. K. et al. Laser-induced graphene interdigitated electrodes for label-free or nanolabel-enhanced highly sensitive capacitive aptamer-based biosensors. *Biosensors and Bioelectronics* **164**, 112272 (2020).
130. Wan, Z. F. et al. Laser induced self-N-doped porous graphene as an electrochemical biosensor for femtomolar miRNA detection. *Carbon* **163**, 385-394 (2020).
131. Tai, M. J. Y. et al. Laser-scribed graphene nanofiber decorated with oil palm lignin capped silver nanoparticles: a green biosensor. *Scientific Reports* **11**, 5475 (2021).
132. Lu, J. et al. MicroRNA expression profiles classify human cancers. *Nature* **435**, 834-838 (2005).
133. Lahcen, A. A. et al. Laser-scribed graphene sensor based on gold nanostructures and molecularly imprinted polymers: Application for Her-2 cancer biomarker detection. *Sensors and Actuators B:Chemical* **347**, 130556 (2021).
134. Rauf, S. et al. Binary transition metal oxide modified laser-scribed graphene electrochemical aptasensor for the accurate and sensitive screening of acute myocardial infarction. *Electrochimica Acta* **386**, 138489 (2021).
135. Yagati, A. K. et al. Silver nanoflower-reduced graphene oxide composite based micro-disk electrode for insulin detection in serum. *Biosensors and Bioelectronics* **80**, 307-314 (2016).
136. Liu, J. J. et al. A novel electrochemical insulin aptasensor: From glassy carbon electrodes to disposable, single-use laser-scribed graphene electrodes. *Bioelectrochemistry* **143**, 107995 (2022).
137. Li, F. et al. Wearable temperature sensor with high resolution for skin temperature monitoring. *ACS Applied Materials & Interfaces* **14**, 43844-43852 (2022).
138. Jung, H. & Lee, H. Semi-transparent reduced graphene oxide temperature sensor on organic light-emitting diodes for fingerprint liveness detection of smartphone authentication. *Sensors and Actuators A:Physical* **331**, 112876 (2021).
139. Han, R. G. et al. Facile fabrication of rGO/LIG-based temperature sensor with high sensitivity. *Materials Letters* **304**, 130637 (2021).
140. Huang, K. et al. Accurate flexible temperature sensor based on laser-induced graphene material. *Shock and Vibration* **2021**, 9938010 (2021).
141. Chen, R. et al. Facile fabrication of a fast-response flexible temperature sensor via laser reduced graphene oxide for contactless human-machine interface. *Carbon* **187**, 35-46 (2022).
142. Jung, H. Reduced graphene oxide temperature sensor via photo-thermal laser irradiation for a printed circuit board. *Materials Letters* **314**, 131758 (2022).
143. Jung, H. & Park, J. Adherable temperature sensor to a porous structure of fiber via reduced graphene oxide and poly(diallyldimethylammonium chloride) complex. *Journal of Micromechanics and Microengineering* **32**, 045001 (2022).
144. You, R. et al. Fabrication of flexible room-temperature NO_2 sensors by direct laser writing of In_2O_3 and graphene oxide composites. *Sensors and Actuators B:Chemical* **277**, 114-120 (2018).
145. Wu, D. Z. et al. A simple graphene NH_3 gas sensor via laser direct writing. *Sensors* **18**, 4405 (2018).
146. Stanford, M. G. et al. Laser-induced graphene for flexible and embeddable gas sensors. *ACS Nano* **13**, 3474-3482 (2019).
147. Zhu, J. X. et al. Biomimetic turbinate-like artificial nose for hydrogen detection based on 3D porous laser-induced graphene. *ACS Applied Materials & Interfaces* **11**, 24386-24394 (2019).
148. Choi, J. et al. Laser-induced graphene on a quartz crystal microbalance for humidity sensing. *Crystals* **11**, 289 (2021).
149. Paterakis, G. et al. Highly sensitive and ultra-responsive humidity sensors based on graphene oxide active layers and high surface area laser-induced graphene electrodes. *Nanomaterials* **12**, 2684 (2022).
150. Cai, J. G. et al. Laser direct writing of a high-performance all-graphene humidity sensor working in a novel sensing mode for portable electronics. *ACS Applied Materials & Interfaces* **10**, 23987-23996 (2018).
151. Li, X. et al. Facile fabrication of laser-scribed-graphene humidity sensors by a commercial DVD drive. *Sensors and Actuators B:Chemical* **321**, 128483 (2020).
152. Zhu, C. C. et al. Graphene oxide humidity sensor with laser-induced graphene porous electrodes. *Sensors and Actuators B:Chemical* **325**, 128790 (2020).
153. Lan, L. Y. et al. One-step and large-scale fabrication of flexible and wearable humidity sensor based on laser-induced graphene for real-time tracking of plant transpiration at bio-interface. *Biosensors and Bioelectronics* **165**, 112360 (2020).
154. Khattak, Z. J. et al. Mass-producible 2D nanocomposite-based temperature-independent all-printed relative humidity sensor. *ACS Omega* **7**, 16605-16615 (2022).
155. Gao, W. et al. Fully integrated wearable sensor arrays for multiplexed in situ perspiration analysis. *Nature* **529**, 509-514 (2016).
156. Kaidarova, A. et al. Wearable multifunctional printed graphene sensors. *npj Flexible Electronics* **3**, 15 (2019).
157. Jung, H. Stability-improved reduced graphene oxide sensors via resistance initialization of laser irradiation for temperature and gas sensing. *Journal of the Korean Physical Society* **80**, 914-919 (2022).
158. Xuan, X. et al. A highly stretchable and conductive 3D porous graphene metal nanocomposite based electrochemical-physiological hybrid biosensor. *Biosensors and Bioelectronics* **120**, 160-167 (2018).
159. Yang, Y. R. et al. A laser-engraved wearable sensor for sensitive detection of uric acid and tyrosine in sweat. *Nature Biotechnology* **38**, 217-224 (2020).
160. Lee, C. W. et al. Fabrication of laser-induced graphene-based multifunctional sensing platform for sweat ion and human motion monitoring. *Sensors and Actuators A:Physical* **334**, 113320 (2022).
161. Chhetry, A. et al. Black phosphorus@laser-engraved graphene heterostructure-based temperature–strain hybridized sensor for electronic-skin applications. *Advanced Functional Materials* **31**, 2007661 (2021).
162. Ye, X. H. et al. Pattern directive sensing selectivity of graphene for wearable multifunctional sensors via femtosecond laser fabrication. *Advanced Materials Technologies* **5**, 2000446 (2020).
163. Li, W. et al. Electrochemistry of individual monolayer graphene sheets. *ACS Nano* **5**, 2264-2270 (2011).
164. Banerjee, S. et al. Electrochemistry at the edge of a single graphene layer in a nanopore. *ACS Nano* **7**, 834-843 (2013).
165. Wu, Q. et al. Triode-mimicking graphene pressure sensor with positive resistance variation for physiology and motion monitoring. *ACS Nano* **14**, 10104-10114 (2020).
166. Gan, Z. S. et al. Three-dimensional deep sub-diffraction optical beam lithography with 9 nm feature size. *Nature Communications* **4**, 2061 (2013).